IMPACTS OF DNA METHYLATION ON H2A.Z DEPOSITION AND NUCLEOSOME STABILITY

Rochelle M. Shih[1], Yasuhiro Arimura[1,2], Hide A. Konishi[1], Hironori Funabiki[1]*
[1] Laboratory of Chromosome and Cell Biology, The Rockefeller University, New York, New York, 10065, USA
[2] Basic Sciences Division, Fred Hutchinson Cancer Center, Seattle, Washington, 98109-1024, USA
*Tel: 1-212-327-7293; Email: funabih@rockefeller.edu

ABSTRACT
In eukaryotes with DNA methylation, the histone variant H2A.Z and DNA methylation are maintained in mutually exclusive sections of the genome. How this antagonism is established, however, remains an open question. Here, we examined the impacts of DNA methylation on both the intrinsic stability of H2A.Z nucleosomes and chaperone-mediated H2A.Z deposition. Cryo-EM and endonuclease accessibility analyses show that H2A.Z nucleosomes with methylated DNA are more open and accessible compared to their unmethylated counterparts. In *Xenopus laevis*, H2A.Z preferentially associates with unmethylated DNA in both the fibroblast cell line XTC-2 and sperm pronuclei formed in the transcriptionally silent egg extract. The proportion of H2A.Z that colocalizes with methylated DNA, however, is higher in sperm pronuclei than in XTC-2. By monitoring nucleosome assembly on synthetic DNA constructs in *Xenopus* egg extracts, we find that the H2A.Z bias for unmethylated substrates is dependent on the SRCAP complex, the major H2A.Z deposition chaperone. Consistently, recruitment of the SRCAP complex to DNA is suppressed by DNA methylation. Altogether, we propose that the SRCAP complex is the major determinant for preferential H2A.Z enrichment on unmethylated DNA, whereas DNA methylation destabilizes DNA wrapping in H2A.Z-containing nucleosomes.

INTRODUCTION
Structural features of the nucleosome, a protein-DNA complex composed of ~146 bp DNA wrapped around a histone octamer, directly affect and regulate genomic accessibility to a diversity of DNA binding proteins, in part, through incorporating histone variants with unique physical properties (Kurumizaka et al., 2021; Talbert and Henikoff, 2016). The highly evolutionarily conserved H2A variant, H2A.Z, is involved in transcriptional regulation with a well described localization at the transcription start sites (TSSs) of active genes (Bönisch and Hake, 2012; Giaimo et al., 2019; Zlatanova and Thakar, 2008). However, while typically associated with gene activation, H2A.Z has also been connected to a range of functions including DNA repair, chromosome segregation, heterochromatin maintenance, and transcriptional repression (Colino-Sanguino et al., 2022; Giaimo et al., 2019). Loss of H2A.Z induces lethality in many eukaryotes, such as mice, *Drosophila*, and *Tetrahymena* (Faast et al., 2001; Liu et al., 1996; Van Daal and Elgin, 1992), and dysregulation of its localization has been linked to several diseases, including various cancers and the developmental disorder Floating-Harbor syndrome (Buschbeck and Hake, 2017; Diegmüller et al., 2025). What mechanisms mediate proper H2A.Z localization, and how that connects with its broad-reaching functions, represents an important area of study.

Genomic sequencing analysis of a wide range of eukaryotes have found H2A.Z and DNA methylation, typically occurring as 5-methylcytosine (5mC), to be strikingly anti-correlated across the genome, at both a global and local level (Berta et al., 2021; Coleman-Derr and

Zilberman, 2012; Conerly et al., 2010; Murphy et al., 2018; Nie et al., 2019; Zemach et al., 2010; Zilberman et al., 2008). The high conservation of this antagonism points to the existence of a shared fundamental pathway involved in creating this dichotomy and emphasizes its functional importance. In *Arabidopsis,* H2A.Z mediates recruitment of the demethylase ROS1, thereby promoting DNA demethylation; however, this pathway uses plant-specific machinery that targets only a particular set of genomic loci (Nie et al., 2019). More general mechanisms for how the mutually exclusive H2A.Z and DNA methylation compartments exist at large remain to be resolved.

DNA methylation may mediate H2A.Z exclusion via two distinct mechanisms: 1) influencing the intrinsic physical stability of the nucleosome, and/or 2) modulating the activity of nucleosome-remodelers. H2A.Z and H2A diverge in sequence along areas important for stabilizing intra-nucleosome interactions, such as the L1 loop, docking domain, and C-terminus (Bönisch and Hake, 2012). DNA methylation can influence the geometry of DNA, particularly its roll and twist, which then likely affect nucleosome wrapping (Li et al., 2022b). A large body of work has been conducted on the physical impacts of either H2A.Z or DNA methylation on the nucleosome, but conflicting conclusions have been reported; incorporation of H2A.Z or DNA methylation independently has been shown to cause stabilizing (Chen et al., 2013; Choy et al., 2010; Collings et al., 2013; Dai et al., 2021; Ishibashi et al., 2009; Lee et al., 2015; Lee and Lee, 2012; Park et al., 2004; Thambirajah et al., 2006), destabilizing (Horikoshi et al., 2019; Jimenez-Useche et al., 2014; Jimenez-Useche and Yuan, 2012; Lee et al., 2015; Li et al., 2023; Ngo et al., 2016; Rudnizky et al., 2016; Weber et al., 2010; Zhang et al., 2005), or no detectable effects (Fujii et al., 2016; Langecker et al., 2015; Osakabe et al., 2015). Nevertheless, it is possible that the combination of H2A.Z and DNA methylation's effects may physically bias against retention of H2A.Z nucleosomes on methylated DNA and contribute to their overall antagonism.

H2A.Z remodeling is primarily carried out by the Ino80 family of nucleosome remodelers. Both the SRCAP complex (SRCAP-C) and Tip60 complex (Tip60-C) mediate exchange of canonical H2A to H2A.Z within a nucleosome (Ruhl et al., 2006), while the Ino80 complex (Ino80-C) has been reported to evict H2A.Z (Scacchetti and Becker, 2021; Watanabe and Peterson, 2010). Tip60-C can also associate with the H2A.Z chaperone, ANP32e, to evict H2A.Z from nucleosomes (Mao et al., 2014; Obri et al., 2014). Members of this remodeler family are prime candidates for enforcing the separation of H2A.Z and DNA methylation; however, it is unknown whether any of these complexes exhibit DNA methylation sensitivity.

To determine molecular mechanisms contributing to the mutual exclusion of H2A.Z and DNA methylation within the genome, here we investigated the effects of DNA methylation on both the physical stability of H2A.Z nucleosomes and remodeler-mediated deposition of H2A.Z onto synthetic DNA constructs by employing cryo-EM structural analysis and the physiological *Xenopus* egg extract system, respectively.

RESULTS

Cryo-EM analysis of H2A.Z nucleosomes in the presence or absence of DNA methylation

To assess the physical impacts of DNA methylation on H2A.Z nucleosomes, we solved cryo-EM structures of human H2A.Z nucleosomes reconstituted with either methylated (Me) or unmethylated (UM) Sat2R-P DNA (**Fig 1, Suppl Fig 1, Suppl Table 1**). The Sat2R-P sequence is

a 152 bp artificial palindromic sequence containing 9 evenly distributed CpG sites and was engineered from a published canonical nucleosome crystal structure containing a methylated derivative of the human satellite II sequence (termed Sat2R) (Osakabe et al., 2015) (**Fig 1A**). This sequence was chosen for two reasons: 1) human satellite II (HSat2) represents a highly abundant methylated sequence which undergoes disease-associated differential methylation (Ehrlich, 2003; Jackson et al., 2004; Tilman et al., 2012; Unoki, 2021; Wong et al., 2001), and 2) the symmetric palindromic sequence was needed to increase final structure resolutions due to the two-fold pseudo symmetry about the nucleosome dyad axis. Prepared nucleosomes were run on a native PAGE gel to assess for quality, where both samples appeared as a singular band with minor comparable populations of unincorporated DNA (**Suppl Fig 1A**).

Cryo-EM structures of UM and Me Sat2R-P H2A.Z nucleosomes were solved at a final resolution of 3.05 Å and 2.78 Å, respectively (**Fig 1B and C, Suppl Fig 1**). We found that the nucleosome dyad was shifted roughly two base pairs from the center of the Sat2R-P palindrome, introducing a sequence asymmetry despite our intended use of the palindromic sequence. The shifted nucleotide positions were determined using the higher resolution densities surrounding the nucleosome dyad, which allowed for pyrimidine and purine distinction (**Suppl Fig 2A-D**). Two atomic models (termed v1 and v2) with mirrored DNA sequences were generated for each structure to account for the resultant sequence asymmetry, with the final EM densities likely reflecting an average of these two models (**Suppl Fig 2E**).

As a whole, both the methylated and unmethylated structures resembled previously published H2A.Z nucleosome structures and exhibited a linker DNA asymmetry where one side of the nucleosome (distal face 2, DF2) contained a highly flexible linker DNA region compared to the other (distal face 1, DF1) (**Fig 1B and C**) (Horikoshi et al., 2013; Lewis et al., 2021; Suto et al., 2000). As a palindromic DNA sequence was used, it is likely that the asymmetrical faces in the cryo-EM structures arose due to an averaging of closed and open H2A.Z nucleosome particles into the same structure rather than representing an asymmetry found in individual particles.

In a direct comparison of DF2 linker DNA lengths, we found that the Me Sat2R-P map had much weaker linker DNA density than UM Sat2R-P, resulting in a ~7 bp shorter resolved DNA model for the methylated structure (**Fig 1D**). This loss of linker density indicates destabilized histone-DNA interactions and increased DNA structural variability in the presence of DNA methylation. Along similar lines, Root Mean Squared Distance (RMSD) analysis identified the H2A.Z-H2B dimer of DF2, as well as the overall DNA backbone, as regions of considerable difference between the methylated and unmethylated structures, whereas DF1, the closed side of the nucleosome with a highly resolved linker DNA, was largely similar between the two (**Fig 1E**).

DNA methylation creates open H2AZ nucleosome structures

To further characterize areas of change, maps of unmethylated and methylated H2A.Z structures were filtered and resampled to the same resolution (~3 Å) for fair comparison (**Fig 2A**). Three major differences between the maps were identified. First, cryo-EM densities of the H3 N-terminus and H2A.Z C-terminus on DF2 were much weaker in the methylated structure as compared to unmethylated, preventing model construction in these areas (**Fig 2B**). Second, an extra density on the H2A.Z-H2B acidic patch was seen on the methylated map but was not present on the unmethylated map (**Fig 2C**). Third, between the two major orientations the H4 N-

terminal tail can adopt (Arimura et al., 2021), the unmethylated map showed a strong preference for the inward orientation whereas the methylated structure exhibited similar populations of inward and outward orientations (**Fig 2D**).

The H3 N-terminus interacts with the H2A/H2A.Z C-terminus and DNA to hold the linker DNA close to the body of the nucleosome (Li et al., 2023; Li and Kono, 2016). Loss of the H3 N-terminal density from the methylated structure suggests destabilized DNA-histone interactions that are consistent with the shorter resolved linker DNA on DF2 of the methylated model compared to unmethylated (**Fig 1D**). The H4 N-terminal tail, on the other hand, mediates inter-nucleosomal interactions through contacts with a neighboring acidic patch (Chen et al., 2017; Luger et al., 1997). The extra density on the Me Sat2R-P acidic patch may then have come from the H4 tail of another nucleosome, in line with the changes also observed in H4 tail orientation. These observations may be consistent with reports that DNA methylation increases condensation of nucleosomes, as well as bare DNA, *in vitro* and *in vivo* (Buitrago et al., 2021; Jimenez-Useche et al., 2014; Yang et al., 2020).

To more quantitatively assess methylation-dependent structural changes, we conducted an *in silico* mixing 3D classification analysis (Arimura et al., 2021; Hite and MacKinnon, 2017) by combining micrographs collected from both methylated and unmethylated nucleosome samples and then sorted particles picked from the combined micrographs into six 3D classes of nucleosomes, each with varying degrees of open or closed linker DNA (**Fig 2E and F, Suppl Fig 3**). Most of the unmethylated particles (>60%) were sorted into the closed linker classes (Class 1 and 2) whereas the majority of methylated particles (~60%) belonged to classes with open linkers (Classes 3, 4, 6) (**Fig 2F**). The fraction of hexasomes (Class 5) is minor in both conditions with a slight increase in methylated particles (Class 5). Among these open linker classes that are preferentially found in methylated particles, class 4 also represents nucleosomes where the palindromic center of the DNA has slid and is considerably offset from the dyad axis of the histone octamer. This may explain the weaker DF2 linker density seen in the high resolution Me Sat2R-P structure (**Fig 1D**). Additionally, the DNA backbone of the methylated nucleosome structure had a lower local resolution compared to unmethylated, despite the methylated map having a higher global resolution (**Suppl Fig 4**). This is consistent with the increased population of open linker and slid nucleosome particles in the methylated structure. Altogether, our cryo-EM structural analysis suggests that the presence of DNA methylation creates open and potentially destabilized H2A.Z nucleosome structures.

Cryo-EM structures of 601L H2A.Z nucleosomes show no difference between methylation status

In addition to the Sat2R-P nucleosomes, we also solved cryo-EM structures of human H2A.Z nucleosomes reconstituted on methylated and unmethylated 601L DNA, a palindromic version of the lefthand portion of the classic Widom 601 sequence (**Suppl Fig 5 and 6, Suppl Table 1**) (Lowary and Widom, 1998). Final maps of the unmethylated and methylated structures were obtained at 3.09 Å and 3.25 Å, respectively (**Suppl Fig 5B-E**). RMSD analysis of the solved structures showed that both maps were essentially identical to each other, with the few differences present localized to highly flexible regions of the nucleosome (**Suppl Fig 5F**). The lack of clear structural differences when using 601L DNA is likely due to its artificially strong

nucleosome positioning ability, which may have prevented detection of subtle changes caused by DNA methylation.

DNA methylation increases accessibility of H2A.Z but not H2A nucleosomes

In order to validate the observed opening of the H2A.Z nucleosome structure by DNA methylation, and to determine if this methylation effect is also present on nucleosomes containing canonical H2A, we measured nucleosome DNA accessibility via restriction enzyme digest (**Fig 3, Suppl Fig 7 and 8**). We tested both human H2A and H2A.Z nucleosomes reconstituted with methylated and unmethylated versions of 152 bp non-palindromic Sat2R DNA that was modified to include a singular HinfI site 18 bp in from the 5'-end containing a Cy5-fluorophore (**Fig 3A**). Homogeneity of the reconstituted nucleosomes was assessed via native PAGE and mass photometry analysis prior to restriction digest analysis (**Suppl Fig 7A-C**). Digest of bare control DNA confirmed that HinfI behaved similarly on both methylated and unmethylated Sat2R substrates over the time scale used in the experiment (**Suppl Fig 7D**). We found that H2A.Z nucleosomes were more accessible to enzymatic digest than H2A nucleosomes, independent of DNA methylation status (**Fig 3B and C, Suppl Fig 8**). When comparing methylation-dependent differences for each type of nucleosome, methylated and unmethylated H2A nucleosomes were largely digested at the same rate. Methylated H2A.Z nucleosomes, on the other hand, exhibited a small but more pronounced increase in accessibility as compared to its unmethylated counterpart (**Fig 3B and C, Suppl Fig 8**). These results corroborate our structural findings and also suggest that the effects of DNA methylation may be negligible on an intrinsically stable nucleosome (i.e. containing H2A) but can further destabilize, in a selective manner, the already open and accessible H2A.Z nucleosome.

H2A.Z and DNA methylation localization in *Xenopus laevis* sperm pronuclei and a fibroblast cell line

Results from our structural and biochemical experiments indicate decreased wrapping stability of H2A.Z nucleosomes on methylated DNA. While functional implications likely exist, this subtle effect on the intrinsic physical stability of the H2A.Z nucleosome is unlikely to be the sole driver of the mutually exclusive H2A.Z and DNA methylation compartmentalization in cells. To identify the major biochemical mechanism underlying this dichotomy, we turned to the *Xenopus laevis* egg extract system, a unique cell-free system that allows for characterization of chromatin proteins under physiological conditions (Jenness et al., 2018; Lohka and Maller, 1985; Postow et al., 2008; Wassing et al., 2024; Xue et al., 2013; Zierhut et al., 2014).

To ensure that *Xenopus* egg extract is a valid tool for studying the H2A.Z-DNA methylation antagonism, we conducted CUT&Tag – Bisulfite Sequencing (CnT-BS) (Li et al., 2021), a method which allows for the direct assessment of DNA methylation on CUT&Tag reads, against H2A.Z of *Xenopus* sperm nuclei incubated in interphase extract. This condition mimics fertilization and allows for full nucleosome assembly onto sperm (primarily composed of protamines and H3/H4 tetramers) to create functional pronuclei (Oikawa et al., 2020). We also collected samples against H3 to serve as a pan-nucleosome control. Since sperm pronuclei in egg extract represents a unique transcriptionally silent state (Engelke et al., 1980; Newport and Kirschner, 1982; Veenstra et al., 1999), we also performed CnT-BS on XTC-2 cells, a *Xenopus*

laevis fibroblast cell line (Pudney et al., 1973), to assess changes in DNA methylation and H2A.Z overlap across different nuclei types.

Initial comparisons of CnT-BS reads across two biological replicates of our four conditions demonstrated good reproducibility between replicates, while each set of experimental conditions exhibited distinct characteristics. A greater than 99 % bisulfite conversion efficiency rate, as assessed through our unmethylated lambda DNA spike-in, was achieved, and correlation matrices of both the mapped reads and methylation calls were highly similar between biological replicates (**Suppl Fig 9, Suppl Table 2 and 3**). When comparing across conditions, for both the H3/H2A.Z mapped reads and DNA methylation sites, the first degree of difference seen was between XTC-2 and sperm samples, and then H3 vs H2A.Z following after, indicating that large-scale changes in the DNA methylation and genomic landscape occurred between the two different nuclear states (**Suppl Fig 9**).

To assess characteristics of H2A.Z and H3 genomic distributions, we subset the *Xenopus* genome into 1,000 bp bins and classified the top 20 % of bins containing the most mapped reads for each condition based on annotated functionalities (Fisher et al., 2023). We found that a greater proportion of highly mapped H2A.Z bins were located near promoter regions as compared to H3 for both sperm and XTC-2 samples (**Suppl Fig 10A**). Although transcription is suppressed in *Xenopus* egg extracts, H2A.Z in sperm pronuclei were well positioned at TSSs, as generally seen for actively transcribed genes in somatic cells (**Suppl Fig 10B and C**). This mirrors the reported deposition of H3K4me3 at the +1 TSS sites in *Xenopus* sperm nuclei prior to remodeling as well as reports in zebrafish sperm and *Drosophila* that H2A.Z is positioned at promoters prior to zygotic genome activation (ZGA) (Ibarra-Morales et al., 2021; Murphy et al., 2018; Oikawa et al., 2020).

H2A.Z is biased towards hypomethylated regions of the genome in both *Xenopus* sperm pronuclei and the XTC-2 fibroblast cell line

We next determined the methylation status of CpGs associated with either H2A.Z or H3 across replicates of XTC-2 and sperm nuclei (**Fig 4A**). One notable drawback of CUT&Tag is a bias towards open and accessible regions (Kaya-Okur et al., 2020; Richard et al., 2025), which may artificially amplify open chromatin signals and lead to an underestimation of DNA methylation status. To circumvent this issue, we analyzed H3 CpG methylation in areas outside of H2A.Z peaks (which tend to be highly accessible) to compare genomic methylation profiles in H2A.Z low/absent regions (H3) vs H2A.Z enriched peaks (H2A.Z).

Overall, sperm chromatin had a higher degree of methylation than XTC-2 chromatin, with 85.3 ± 0.4 % *s.d.* of CpGs in H3 reads experiencing methylation in sperm compared to 53.5 ± 0.4 % in XTC nuclei (**Suppl Table 2**). Methylated CpG frequencies of H2A.Z-associated reads were reduced to 43.0 ± 0.7 % in sperm chromatin and even further down to 3.0 ± 0.3 % in XTC-2 cells. Mapping of H3 associated methylation calls to annotated genes of the *Xenopus laevis* genome showed ubiquitous distribution of methylation across the length of genes, except for at the TSSs where there was a marked depletion of methylation (**Suppl Fig 10B and C left**). Nearly all of these H3-marked hypomethylated TSSs exhibited H2A.Z enrichment in both sperm pronuclei and XTC-2 (**Suppl Fig 10B and C right**), indicating that hypomethylation-exclusive positioning of H2A.Z is most prominent at the TSSs (**Suppl Fig 10D**).

DNA methylation-sensitive H2A.Z deposition on synthetic DNA constructs in *Xenopus* egg extract

To directly test whether the presence or absence of DNA methylation can dictate preferential H2A.Z deposition independently of other pre-existing epigenetic marks or DNA sequence, we took advantage of the *Xenopus* egg extract's ability to efficiently assemble nucleosomes *de novo* onto naked DNA templates (Laskey et al., 1977) (**Fig 4B**). We found that, upon incubation of DNA coated magnetic beads in interphase egg extract, H2A.Z accumulated less efficiently on methylated DNA substrates compared to unmethylated (**Fig 4C and D, Suppl Fig 11**), whereas this methylation-sensitive deposition was not seen for H2A.X-F, the predominant H2A histone variant in *Xenopus* egg extract (**Fig 4E and F, Suppl Fig 11**) (Shechter et al., 2009). The methylation bias of H2A.Z held true for arrays of either the GC-rich Widom 601 (57 % GC content) or the more AT-rich human HSat2 (38% GC content) sequence. We next asked whether both H2A.Z variants, H2A.Z.1 and H2A.Z.2 (H2A.V), exhibit the same DNA methylation sensitivity. Since our antibody does not distinguish between the two H2A.Z paralogs, we translated ALFA-tagged (Götzke et al., 2019)versions of the variants in egg extract from exogenously added mRNA and found that both paralogs displayed preferential deposition onto unmethylated DNA (**Suppl Fig 12**).

The SRCAP complex mediates H2A.Z's preferential deposition on unmethylated DNA

Since SRCAP-C is known to play a major role in depositing H2A.Z to nucleosomes via exchange of H2A dimers on the nucleosome with H2A.Z (Ruhl et al., 2006), we examined if the observed preferential association of H2A.Z with unmethylated DNA in *Xenopus* egg extracts is mediated by SRCAP-C. Depletion of SRCAP-C from extract using a custom antibody against *Xenopus laevis* SRCAP greatly reduced the amount of H2A.Z associated with unmethylated DNA compared to control depletion (ΔIgG), while its levels on methylated DNA were not affected (**Fig 5A-C, Suppl Fig 13A**). Consequently, in SRCAP-C-depleted (ΔSRCAP) extracts, residual H2A.Z binding to DNA became insensitive to DNA methylation status, while the amount of H2A.X-F on DNA was not affected by SRCAP-C depletion (**Fig 5B and D, Suppl Fig 13A**). Consistent with the critical role of SRCAP-C in the preferential deposition of H2A.Z to unmethylated DNA, DNA-binding of SRCAP and ZNHIT1, two core subunits of SRCAP-C, was greatly inhibited by methylation in egg extract (**Fig 5E-F, Suppl Fig 13B**). In contrast, p400, the ATPase of Tip60-C, did not exhibit methylation-sensitive DNA binding (**Suppl Fig 14**). From these results, we conclude that SRCAP-C is the major driver biasing H2A.Z deposition against methylated DNA.

DISCUSSION

In this study, we found that DNA methylation can affect H2A.Z deposition and stability via two distinct mechanisms (**Fig 6)**. DNA methylation directly opposes H2A.Z deposition by inhibiting SRCAP-C DNA binding. SRCAP-C accounts for the majority of H2A.Z deposition on unmethylated DNA and is the primary mediator behind DNA methylation's exclusion of H2A.Z in the transcriptionally inactive *Xenopus* egg extract. A subpopulation of H2A.Z, however, is still deposited onto methylated DNA, driven by methylation insensitive mechanism(s) whose identity remains to be established. Once formed, H2A.Z nucleosomes on methylated DNA are more open and accessible compared to their unmethylated counterparts. This decrease in DNA-

histone contact stability of methylated H2A.Z nucleosomes may then further facilitate clearance of H2A.Z from methylated regions of the genome.

Supporting our observation that a SRCAP-independent mechanism(s) exists to deposit H2A.Z on methylated DNA in *Xenopus* egg extract, a substantial fraction (~40%) of H2A.Z-associated genomic DNA is methylated in sperm pronuclei. In the fibroblast cell line XTC-2, that methylated H2A.Z fraction is greatly reduced to 3%. However, due to the accessibility bias inherent within CUT&Tag, our data likely underestimates the true degree of H2A.Z and DNA methylation overlap, particularly in the XTC-2 samples. For comparison, a previous study in human myometrium reported that ~20% of CpGs overlapping with H2A.Z are methylated, indicating that a sizeable population of colocalized H2A.Z and DNA methylation exists in somatic cells which warrants further investigation (Berta et al., 2021). Nevertheless, we believe the decreased trend in H2A.Z and DNA methylation overlap of XTC-2 cells holds true and suggests that the high degree of H2A.Z and DNA methylation coincidence in sperm pronuclei reflects its unique early development and/or transcriptionally silent state. Given the strong preference of SRCAP-C binding to unmethylated DNA in *Xenopus* egg extracts, we predict that additional pathways missing in the egg extract system are necessary to reinforce the antagonism between DNA methylation and H2A.Z enrichment.

Perhaps the greatest difference between XTC-2 cells and *Xenopus* eggs is the presence of transcription, which is one of the main evictors of H2A.Z and necessary for global H2A.Z turnover as well as pruning of randomly deposited H2A.Z within gene bodies (Hardy et al., 2009; Lashgari et al., 2017; Ranjan et al., 2020; Tramantano et al., 2016). Traversing of RNA polymerase (Pol) II across nucleosomes, aided by the FACT complex, results in transient histone dimer displacement (Belotserkovskaya et al., 2003; Bevington and Boyes, 2013; Bintu et al., 2011; Kireeva et al., 2002), leading to the possibility that the more accessible H2A.Z nucleosome structures formed on methylated DNA may have increased susceptibility to Pol II disruption. Furthermore, FACT and Spt6 do not reincorporate H2A.Z into the reassembled nucleosome post Pol II encounter, reinforcing selective loss of H2A.Z (Heo et al., 2008; Jeronimo et al., 2015). Outside of transcription, the egg extract system also lacks both the DNMT3 enzymes responsible for *de novo* methylation and the TET system responsible for DNA methylation removal in animals (Wühr et al., 2014b). In *Arabidopsis*, H2A.Z promotes ROS1-associated DNA demethylation (Nie et al., 2019) and must be excluded to ensure faithful heterochromatin formation (Zhou et al., 2023). Thus, H2A.Z-driven mechanisms to limit DNA methylation remain relevant pathways to increase the H2A.Z/DNA methylation separation within the genome which may be missing in eggs/early embryonic states.

Exactly how SRCAP-C senses DNA methylation remains a pertinent question. Recent structural work on the yeast SWR1 complex and human SRCAP-C indicate that both the ATPase and the ZNHIT1 subunit (Swc6 in yeast) mediate binding of, and one-dimensional diffusion on, naked DNA substrates (Louder et al., 2024; Park et al., 2024), marking them as likely candidates responsible for methylation sensing. Additionally, the YEATS domain-containing subunit GAS41, found in both SRCAP-C and Tip60-C, recognizes H3K14ac and H3K27ac (Hsu et al., 2018a, 2018b), and deposition of H3K27ac, itself, is antagonized by DNA methylation at enhancers (King et al., 2016). It is possible that both direct recognition of DNA methylation and changes in the PTM landscape of methylated chromatin play a role in dictating SRCAP-C localization and activity.

Although a consensus on how DNA methylation influences nucleosome stability has yet to be achieved, our results indicate that DNA methylation creates more open nucleosome structures, particularly on H2A.Z nucleosomes, similar to reports from FRET-based and molecular simulation studies on the canonical H2A nucleosomes (Jimenez-Useche et al., 2014; Jimenez-Useche and Yuan, 2012; Li et al., 2022a; Ngo et al., 2016). Although the ambiguity in DNA positioning of our cryo-EM structures prevents us from discussing the structural coordination of specific CpG sites, we favor the idea that the increase in accessibility is due to effects of DNA methylation on global DNA structure rather than at specific methylated segments. This is in line with observations that methylation increases overall DNA stiffness, making it harder for the DNA to bend and wrap around histone octamers (Ngo et al., 2016; Pérez et al., 2012).

Our restriction enzyme accessibility assay shows that H2A.Z nucleosomes are considerably more open and accessible compared to canonical H2A, regardless of methylation status. This difference is substantially larger than that induced by DNA methylation on H2A.Z, suggesting that the physical influence of DNA methylation on nucleosomes is overall subtle. This apparent subtlety, however, may be due to the internal placement of the cut site that we tested, and thus the effect of DNA methylation was preferably observed on an already destabilized nucleosome with H2A.Z. Similar findings have been reported on canonical H2A 601 nucleosomes, where the effects of DNA methylation manifest greatest on an open nucleosome sub-population compared to their closed counterparts (Jimenez-Useche and Yuan, 2012). This is likely why we saw no methylation-dependent structural differences with the 601L sequence (**Suppl Fig 5**), as its innate nucleosome wrapping and positioning ability is even stronger than the classic Widom 601. Overall, we suggest that the subtle nucleosome destabilization effect of DNA methylation is selectively pronounced on H2A.Z nucleosomes, which already exhibit an intrinsic instability compared to canonical H2A nucleosomes.

Beyond its interaction with DNA methylation, we show that H2A.Z promoter localization occurs immediately upon conditions mimicking fertilization in a transcription-independent manner. Unlike the almost complete loss of histones seen in mammalian sperm (Ward and Coffey, 1991; Wykes and Krawetz, 2003), *Xenopus* sperm is packaged as a mixture of protamines and H3/H4 tetramers with very low levels of H2A/H2B dimers, which are then remodeled into full nucleosomes upon fusion with an egg (Katagiri and Ohsumi, 1994; Mann et al., 1982; Oikawa et al., 2020). In our egg extract system, which lacks the maternal genome, we expect the bulk of H2A.Z in sperm pronuclei to be newly deposited and find that H2A.Z is still specifically targeted to promotors either via underlying sequence motifs (Ibarra-Morales et al., 2021; Murphy et al., 2018) or tetramer modifications maintained in sperm (Oikawa et al., 2020). This is similar to *Drosophila* where H2A.Z is recruited to TSSs prior to both Pol II binding and ZGA, marking genes for zygotic activation (Ibarra-Morales et al., 2021), indicating conservation of this initial transcription-independent H2A.Z positioning across both vertebrates and invertebrates.

Our work here provides a critical step in the pathways dictating genomic organization by uncovering the previously undescribed methylation sensitivity of SRCAP-C along with the destabilizing effects of DNA methylation on H2A.Z nucleosomes. Together, these findings provide molecular mechanisms driving the conserved antagonism between H2A.Z and DNA methylation in the genome. However, many questions remain to be answered, such as why the existence of both methylation sensitive and insensitive H2A.Z deposition pathways, the broader functional implications of the H2A.Z-DNA methylation antagonism as a whole, and mechanisms

driving its maintenance in species that experience periods of global demethylation. These questions represent important areas of future study for our understanding of epigenome dynamics throughout development.

MATERIALS AND METHODS

Histone purification and refolding

pET3 vectors containing sequences for human histones H2A, H2A.Z, H2B, H3.2, and H4 (gifts from Shixin Liu) were expressed in Rosetta (DE3) cells (Novagene, Cat# 70954). Cells were pelleted 4000 x *g*, 20 min, 4 °C and resuspended in wash/lysis buffer [50 mM Tris-HCL pH 7.5, 100 mM NaCl, 1 mM EDTA, 5 mM β-mercaptoethanol, 0.2 mM PMSF] + 1 % Triton-X-100 then sonicated. Inclusion pellets were spun 25,000 x *g*, 20 min, 4 °C, and incubated with DMSO at room temperature (RT) for 30 min. Pellets were then resuspended in unfolding buffer [20 mM Tris-HCl pH 7.5, 7 M guanidine-HCl, 10 mM DTT], sonicated until pellets were fully broken up, and re-pelleted at 25,000 x *g*, 20 min, RT. The supernatant was then collected and dialyzed in urea dialysis buffer overnight at 4 °C [10 mM Tris-HCl pH 7.5, 7 M Urea, 1 mM EDTA, 5 mM β-mercaptoethanol, 100 mM or 200 mM NaCl for H2A/H2B and H3/H4, respectively]. Samples were then pelleted at 25,000 x *g*, 20 min, RT and the supernatant passed through Q Sepharose Fast Flow resin (Cytiva, Cat# 17051010). The flow-through was then collected and added to SP Sepharose Fast Flow resin (Cytiva, Cat# 17072910), washed with urea dialysis buffer, and eluted with elution buffer [10 mM Tris-HCl pH 7.5, 7 M Urea, 1 mM EDTA, 600 mM NaCl, 5 mM β-mercaptoethanol].

Equimolar ratios of histones for either octamer, or dimer and tetramer preparation were then mixed and dialyzed into refolding buffer [10 mM Tris-HCl pH 7.5, 1 mM EDTA, 5 mM β-mercaptoethanol, 2 M or 500 mM NaCl for octamers or dimers/tetramers, respectively]. Refolded histones were then purified via FPLC (ÄKTA pure, Cytiva, Cat# SN2626712) (Superdex 200 10/300 GL increase column, Cytiva, Cat# 28990944).

Generation of DNA arrays

Generation of HSat2 arrays for use in chromatinization assays or arrays of Sat2R-P halves to prepare palindromic sequences for cryo-EM analysis was done as previously described in (Dyer et al., 2003). Briefly, DNA sequences of interest (see **Table 1**) containing one BglII site, one BamHI site, and two EcoRV sites surrounding the sequence were generated and purchased from Integrated DNA Technologies (IDT™) and cloned into the pUC18 vector just downstream of the XbaI site. The plasmid was then digested with either XbaI (NEB Cat# R0145) and BglII (NEB Cat# R0144) (to obtain the vector) or BglII and BamHI (NEB Cat# R3136) (to obtain the insert), and agarose gel purified. Vector and insert DNA were then ligated with T4 DNA ligase (NEB Cat# M0202). The digest and ligation steps were repeated until the desired repeat number was achieved.

Palindromic DNA preparation for Cryo-EM

Arrays of Sat2R-P halves were generated as described above. Plasmid containing an array of 601L halves (601L-145-8X) was a gift from Curt Davey (Addgene plasmid # 158572; http://n2t.net/addgene:158572; RRID: Addgene_158572) (Chua et al., 2012a). Arrays of

palindromic DNA halves for Cryo-EM analysis were then digested with EcoRV (NEB Cat# R3195) and purified via PEG precipitation (0.5 M NaCl, 8 % w/v PEG8000). Supernatant were collected and further purified via phenol-chloroform extraction. Insert ends were dephosphorylated with QuickCIP (NEB Cat# M0525) and phenol-chloroform extracted. Samples were then digested with either HinfI (NEB Cat# R0155) (601L DNA) or AvaI (NEB Cat# R0152) (Sat2R-P DNA), phenol-chloroform extracted, and FPLC purified in 1xTE buffer (Superdex 200 10/300 GL increase column, Cytiva, Cat# 28990944). DNA halves were then incubated with T4 DNA ligase (NEB Cat# M0202) per manufacturer's protocol until all halves were completely ligated.

Methylation of DNA substrates

DNA substrates were enzymatically methylated using the *M.SssI* CpG methyltransferase (NEB, Cat# M0226). Approximately 160 U of methyltransferase were used for 50 µg of DNA in 1x NEB 2 buffer with 500 µM SAM. Samples were incubated at 37 °C for at least one hour. Completion of methylation was checked using the methylation sensitive restriction enzyme BstUI (NEB, Cat# R0518). DNA was purified using phenol-chloroform extraction prior to use.

Nucleosome Reconstitution

DNA and either histone octamers or dimers and tetramers were mixed at a final target concentration of 1 µM in 1x TE buffer and 2 M NaCl. Exact ratios of DNA to histones were titrated for each reconstitution batch, starting at equimolar ratios. Samples loaded in dialysis buttons were then added to high salt dialysis buffer [10 mM Tris-HCl pH 7.5 at 4 °C, 1 mM EDTA, 2 M NaCl, 0.01 % Triton X-100, 5 mM β-mercaptoethanol] at 4 °C. The high salt dialysis buffer was then exchanged into low salt dialysis buffer [10 mM Tris-HCl pH 7.5 at 4°C, 1 mM EDTA, 50 mM NaCl, 0.01 % Triton X-100, 5 mM β-mercaptoethanol] at a rate of ~0.7 ml/min over a period of 30-40 h. Nucleosome quality was assessed on a 5 % 37.5:1 acrylamide/bis 0.5 x TBE gel (120 V).

Mass Photometry Analysis of Nucleosomes

Mass photometry analysis was performed on a Refeyn Two^{MP} instrument and analyzed using DiscoverMP v2022R1 (with IScat v1.52.0 and IScat Utils v1.43.0). 24 x 50 mm with 170 ± 5 µm thickness No. 1.5H glass slides (ThorLabs, Cat# CG15KH1) and silicone gaskets (Grace Bio-labs, Cat# 103250) were washed 2x with alternating 100 % isopropanol and deionized water. Clean gaskets were then placed on the cleaned slides to serve as a sample chamber. 5 µl of 1x PBS was placed in the gasket to calibrate each sample collection then 5 µl of nucleosome samples were added for a target final concentration of ~5-10 ng/µl nucleosomes in the well. Measurements were conducted at room temperature.

Cryo-EM Sample Preparation and Data Collection

Human H2A.Z nucleosomes were reconstituted on either 601L or Sat2R-P DNA as described above with a final concentration aim of 1.6 µM in 1 ml. Reconstituted nucleosomes were dialyzed into buffer containing 10 mM HEPES-KOH pH 7.4 and 30 mM KCl then concentrated to a final concentration of ~1 mg/ml using Amicon® Ultra Centrifugal Filters (Cat# UFC5010). Samples were then mixed with 10x cryo-protectant buffer [10 mM HEPES-KOH pH 7.5, 30 mM KCl, 10 % Trehalose, 1 % Hexanediol, 1 mM $MgCl_2$] and 3 µl of each solution was applied to

plasma-cleaned) Quantifoil gold R1.2/1.3 400-mesh grids (Quantifoil) either graphene coated (graphene coating was done in-house as specified in (Arimura et al., 2025) or not for the Sat2R-P and 601L samples, respectively. Grids were then vitrified using the Vitrobot Mark IV (FEI) at 100 % humidity, 2 sec blotting time, blot force 1. Data collection was conducted using the Titan Krios (ThermoFisher), equipped with a 300 kV field emission gun and a K3 direct electron detector (Gatan), at a magnification of x81,000 (0.86 Å/pixel). Total micrographs collected for each sample as follows: 4544 for unmethylated Sat2R-P nucleosomes; 6891 for methylated Sat2R-P; 7020 for unmethylated 601L; 5427 for methylated 601L. Data statistics summarized in **Suppl Table 1**.

Cryo-EM Data Analysis

Diagrams of analysis workflows are shown in **Suppl Fig 1** and **Suppl Fig 5**. Micrographs were motion-corrected using MotionCor2 (Zheng et al., 2017) in Relion v4 (Scheres, 2012). Downstream analysis was conducted in CryoSPARC v4.6 (Structura Biotechnology Inc.). Motion-corrected micrographs then underwent patch CTF correction. Particles were picked using Topaz v0.2 (Bepler et al., 2019) trained on a set of 1,000-2,000 manually picked nucleosome-like particles and then extracted to 384 pix (~330 Å) boxes with 4x binning and used for 2D classification into 200-250 classes. Particles from selected classes were then run through a series of heterogeneous refinements with 1-2 nucleosome-like models and 4 decoy models generated through *ab initio* reconstruction to sort out junk particles from those containing nucleosomes. The heterogenous refinements were iterated until greater than 90 % of particles in the round were classified as nucleosome-like. These particles were then further refined either via Refine 3D, CTF refinement, and polishing in Relion v4 (601L structures) or homogeneous and non-uniform refinements in CryoSPARC v4.6 (Sat2R-P). Particles for the methylated Sat2R-P structure underwent another heterogeneous refinement using a closed nucleosome, open, and hexasome model as starting classes to select for the highest resolved closed nucleosome structure. Final resolutions were determined using the gold standard FSC threshold (FSC = 0.143). Local resolution maps shown in **Suppl Fig 3** were generated using the local resolution estimation tool with default parameters in CryoSPARC. The maps were then visualized on density maps filtered using the local filter tool with default parameters. For the *in silico* mixing 3D classification analysis (**Suppl Fig 4**): micrographs from both unmethylated and methylated Sat2R-P structures were merged and subjected to the data analysis pipeline described above. Six starting models representing different nucleosome structure types were then constructed using the ab initio 3D reconstruction tool. These models were then used as input volumes, and cleaned particles from the merged analysis were then sorted to each of these models using the heterorefinement tool in CryoSPARC.

Atomic Modeling and RMSD analysis

Initial atomic models were generated using previously published structures of human H2A.Z-containing histone core (PDB ID: 3WA9) (Horikoshi et al., 2013) and modified versions of either 601L DNA (PDB ID: 3UT9) (Chua et al., 2012b) or Sat2R DNA (PDB ID: 5CPI) (Osakabe et al., 2015). Models were docked into the EM density maps using Phenix v1.21, then iteratively refined and assessed in Phenix v1.21 (Liebschner et al., 2019) and *Coot* 0.9.8.7 (Emsley et al., 2010). RMSD values were calculated in PyMOL v2.5.7 (Schrödinger) using the cealign function. For the Sat2R-P models, DNA positioning was determined using the EM densities at the dyad of the

unmethylated map which allowed for pyrimidine and purine distinction. A two-base pair shift was determined by assessing ambiguity of densities around nucleotides which change from purine to pyrimidine, and *vice versa*, between mirrored DNA models versus those which retain identity. After determining best-fit DNA models for the unmethylated structure, the same DNA positionings were then used for the methylated structure.

DNA Preparation for Restriction Digest Assay

Non-palindromic 1HinfI_Sat2R DNA (**Table 1**) was prepared via PCR using Q5 polymerase (NEB Cat# M0491). Final concentrations of reaction mixture as follows: 1x Q5 reaction buffer; 200 µM dNTPs; 2 µM forward and reverse primers; 0.2 g/µl DNA template; 0.02 U/µl Q5 polymerase. Roughly 60-65 PCR cycles were run following manufacturer's protocol with a melting temperature of 60 ºC. PCR products were phenol-chloroform extracted and then FPLC purified in 1xTE buffer (Superdex 200 10/300 GL increase column, Cytiva, Cat# 28990944).

Restriction Digest Assay

Nucleosomes were mixed at 30 ng per timepoint sample in 1x rCutSmart® buffer (NEB Cat# B6004S) [50 mM potassium acetate, 20 mM Tris-acetate pH 7.9 at RT, 10 mM magnesium acetate, 100 µg/ml recombinant albumin] and 0.5 U/µl HinfI restriction enzyme (NEB Cat# R0155S). Samples were incubated at 37 ºC and added to stop buffer [final concentrations: 20 mM Tris-HCl pH 8.0 at RT, 20 mM EDTA, 0.1 % SDS, 0.6 mg/ml Proteinase K] at each timepoint. Stopped samples were then incubated at 55 ºC for 40 min and run on a 10 % 37.5:1 acrylamide/bis 0.5x TBE gel (55 min at 150 V) and stained with SYBR™ Safe DNA stain (Thermo Fisher Scientific, Cat# S33102). Fluorescent signals were measured on a LI-COR Odyssey M system and quantified using ImageJ via histogram analysis as previously described in (Stael et al., 2022). The ratio of Cy5: SYBR™ Safe signals was then determined for each time point and plotted. A two-tailed t-test assuming unequal variance was then performed on data from n = 5 experiments for statistical analysis.

Antibodies

Antibodies used in this study are listed in **Table 2**. Custom antibodies were generated through Cocalico Biologicals, Inc.™ using their standard protocol. Target binding of the H2A.Z antibody used for CnT-BS and SRCAP custom antibody in *Xenopus* egg extract was verified using mass spectrometry analysis (MS) (**Supplementary Data 1 and 2**).

Mass Spectrometry Validation

For the MS analysis, 20 µl of antibody-bound Protein A Dynabeads™ (Invitrogen, Cat# 10008D) (0.8 µg antibody per 1 µl of beads) were incubated at a 1:1 ratio with CSF egg extract (see next section) at 4 ºC for 1h. Samples were collected via magnet and washed 3 times with sperm dilution buffer (SDB) [150 mM Sucrose, 10 mM HEPES-KOH pH 8.0, 1 mM $MgCl_2$, 100 mM KCl] then run on a 4-20% gradient SDS-PAGE gel as a 1 cm short-stack. The gel was then stained with Coomassie Brilliant Blue G-250 (Thermo Fisher) and the short stack was cut out. The cut gel was then destained using a solution of 30 % acetonitrile and 100 mM ammonium bicarbonate in water and dehydrated using 100 % acetonitrile. Samples were subjected to heat assisted (50 ºC) trypsinization for 1 h. The resulting peptides were extracted three times with a solution of 70 %

acetonitrile and 0.1 % formic acid then concentrated using a SpeedVac and resuspended in 10 µl volumes. 3 µl of purified peptides were subsequently analyzed by LC-MS/MS using a Dionex 3000 HPLC system equipped with an EasySPrayer (ES902), coupled to an Orbitrap ASCEND mass spectrometer from Thermo Scientific. Peptides were separated by reversed-phase chromatography using solvent A (0.1 % formic acid in water) and solvent B (80 % acetonitrile, 0.1 % formic acid in water) across a 45-min gradient. Data was processed using ProteomeDiscoverer 1.4 and quantified using ProteomeDiscoverer v1.4/Mascot v3.1. The spectra were then queried against a *Xenopus laevis* database (Wühr et al., 2014a) and matched peptides filtered using a Percolator calculated FDR of 1 %. As proxy for protein amount, the average area of the three most abundant peptide signals was used. Relative enrichment of proteins in the sample was then calculated by dividing by known protein concentrations in *Xenopus laevis* eggs and then the enrichment over IgG control was calculated. Common contaminates were marked in red.

***Xenopus laevis* frogs and preparation of sperm and CSF egg extract**

Female *Xenopus laevis* frogs were purchased from Xenopus 1. Male frogs were purchased from either Xenopus 1 (for use in non-sequencing experiments) or the National Xenopus Resource (*XLa.J-Strain*^{NXR}, Cat# NXR_0024; for use in sequencing experiments). Vertebrate animal protocols (20031 and 23020) approved by the Rockefeller University Institutional Animal Care and Use Committee were followed for housing and care.

CSF egg extract and demembranated sperm nuclei were prepared as specified previously (Tutter and Walter, 2006).

Sperm Pronuclei Preparation

Sperm from J-strain frogs were added to prepared CSF egg extract at a final concentration of 1,500 sperm/µl extract with a total extract volume of 200 µl for each sample. 90 ng (~1 % of total DNA) of lambda DNA (Promega Cat# D1521) was also added to assess bisulfite conversion efficiency and the extract solution was then cycled to interphase with the addition of $CaCl_2$ to a final concentration of 0.3 mM and incubated at 20 ºC for 90 min. Samples were then diluted 1:4 with 1xDB3 buffer [10 mM HEPES-KOH pH 8.0, 100mM NaCl, 0.5 mM spermine, 0.5 mM spermidine, 1 mM ASEBF (GoldBio Cat#A-540-1), 1x ROCHE cOmplete™ protease inhibitor cocktail (Cat# 11697498001), 200 mM Sucrose, 0.1 % Tween-20], layered onto 1 ml of 60SDB3 [1xDB3 + 60 % sucrose] and centrifuged at 4 ºC, 10,000 rpm for 45 min (Beckman Coulter SX241.5 rotor). Sample pellets were washed 2x with 1xDB3, centrifuging at 4,000 x *g*, 4 ºC for 4 min, then resuspended in 1x CnT-WB [20 mM HEPES-KOH pH 7.8, 150 mM NaCl, 0.5 mM spermidine, 1x ROCHE cOmplete™ protease inhibitor cocktail, 0.1 % Tween-20].

XTC-2 Cell Line

XTC-2 cells (gift from Dr. David Shechter) were cultured in Leibovitz's L-15 Medium (Gibco™, Cat# 11415064) (0.7x amphibian strength, diluted with cell culture grade water (Corning®, Cat# 46-000-CV)) supplemented with 500 U/ml each of penicillin and streptomycin (Gibco™, Cat# 15140122), and 10 % FBS (R&D systems, Cat# S11150). XTC-2 cells were cultured in a 26 °C incubator without CO_2 supply. Cell line identity was verified via mitotic-spread karyotyping.

XTC-2 Nuclei Preparation
XTC-2 cells were harvested at 90-100 % confluency from a 15 cm dish. Nuclei isolation was performed at 4 ºC using the Nuclei EZ Prep kit (Millipore Cat# NUC101-1KT) as per manufacturer's protocol and resuspended in 1x CnT-WB. For each sample, 18 ng (~1 % of total DNA) of unmethylated lambda DNA (Promega Cat# D1521) was added to 300,000 nuclei to assess for bisulfite conversion efficiency.

Purification of Tn5
Tn5 was purified as described in (Soroczynski et al., 2024). Briefly, VR124 pETv2-10His-pG-Tn5 (E54K, L372P) *E. coli* strain (Addgene #198468) were cultured to log growth phase and Tn5 expression induced with IPTG addition. Cells were harvested at 8,000 x *g*, 30 min at 4 ºC, washed with ice-cold DPBS, re-pelleted and frozen. Frozen pellets were then resuspended at 4 ºC in lysis buffer LysEQ [20 mM HEPES pH 7.8, 800 mM NaCl, 20 mM imidazole, 10 % glycerol, 1 mM EDTA, 2 mM TCEP-HCl, 1x EDTA-free cOmplete protease inhibitor] and sonicated. Lysates were pelleted at 20,000 x *g*, 35 min at 4 ºC, then filtered through a 0.45 µm PES filter. Supernatant was then loaded onto a HisTrap HP 5 ml column (Cytiva, Cat# 17-5247-01) pre-equilibrated with LysEQ buffer. The loaded column was then washed with 10 column volumes each of WashB1 [20 mM HEPES pH 7.8, 800 mM NaCl, 30 mM imidazole, 10 % glycerol, 1 mM EDTA, 2 mM TCEP-HCl] and WashB2 [20 mM HEPES pH 7.8, 800 mM NaCl, 45 mM Imidazole, 10 % glycerol, 1 mM EDTA, 2 mM TCEP-HCl]. Protein was then eluted with EluB [20 mM HEPES pH 7.8, 800 mM NaCl, 400 mM imidazole, 10 % glycerol, 1 mM EDTA, 2 mM TCEP-HCl]. Tn5-containing fractions were pooled and dialyzed 4 ºC overnight in SECB buffer [50 mM Tris-HCl pH 7.5, 800 mM NaCl, 10 % glycerol, 0.2 mM EDTA, 2 mM DTT] then filtered through a 0.45 µm PES filter and FPLC purified on a HiLoad 16/600 Superdex 200 pg column (Cytiva, Cat#: 28989335). Purified fractions were pooled and concentrated with a 30 MWCO Amicon Ultra Centrifugal filter (final concentration 12 µM) and mixed with UltraPure glycerol to a final concentration of 55 % glycerol. Purified Tn5 was stored at -20 ºC.

CUT&Tag-Bisulfite Library Preparation
Sequencing libraries were prepared as previously described in (Li et al., 2021). Briefly, prepared nuclei samples were bound to 10 µl of activated concanavalin A beads (EpiCypher Cat# 21-1401) and incubated with specified primary and secondary antibodies (**Table 2**) in 50 µl Antibody Binding Buffer [CnT-WB + 2 mM EDTA + 0.1 % w/v BSA] for 1 h shaking at RT, washing 3x with CnT-WB between each incubation. Samples were then incubated with 50 µl of transposome complex (1:1 pG-Tn5:adaptor primer mix, ~0.1-0.2 µM final to each sample) in CnT-300 [CnT-WB with 300 mM NaCl] for 1 h at RT then washed with CnT-300. Transposome activity was initiated with addition of 300 µl Tagmentation Buffer [20 mM HEPES-KOH pH 7.8, 300 mM NaCl, 0.5 mM spermidine, 10 mM $MgCl_2$, 1x ROCHE cOmplete™ protease inhibitor cocktail, 0.1 % Tween-20] and incubated 37 ºC, 1500 rpm on thermomixer, 1 h. Reactions were stopped with addition of stop buffer [15 mM EDTA, 0.1 % SDS, 0.2 mg/mL Proteinase K final concentrations] and incubated at 55 ºC overnight, then phenol-chloroform extracted. Purified samples were resuspended in 11 µl of 10 mM Tris-HCl, pH 8.0 and oligonucleotide replacement/gap repaired carried out through addition of 2 µl of 10 µM Tn5mC-ReplO1 DNA oligo (**Table 1**), 2 µl 10x

Ampligase Buffer (Lucigen), 2 µl dNTP mix (2.5 mM for each dNTP). Solutions were subject to the following heating protocol: 50 °C 1 min, 45 °C 10 min, cool to 37 °C at -0.1 °C/second. Once at 37 °C, 3U of T4 DNA polymerase and 12.5U of Ampligase (Lucigen) were added and samples incubated for 30 min. Reactions were stopped with 20 mM EDTA final and purified using the MinElute PCR purification kit (Qiagen Cat# 28004). Samples were bisulfite converted using the EZ DNA Methylation-Lightning Kit (Zymo Research Cat# D5030) and libraries amplified (14 cycles) using NEBNext Q5U Master Mix (NEB Cat# M0597) and Illumina Nextra i5/i7 adapter primers.

Sequencing Data Analysis

Adapter trimming, deduplication, and genome alignment. Libraries were sent to Novogene for sequencing on the NovaSeqX Plus system (PE150). XTC-2 data was then downsampled to 30 million reads using seqtk (v1.5-r133) to have all samples at similar read depths. Adapter trimming and dedeuplication of the demultiplexed reads was then done using fastp v0.24.0 (Chen, 2023) [--adapter_sequence CTGTCTCTTATACAC --adapter_sequence_r2 CTGTCTCTTATACAC -g --poly_g_min_len 5 -p -l 20 --cut_tail -y -Y 20 -q 20 –dedup]. Processed reads were then aligned to the *Xenopus laevis* genome (Xenla 10.1) and methylated CpG proportions for all mapped reads calculated using Bismark v0.24.2 (Krueger and Andrews, 2011) [-q --local --score-min G,20,8 --ignore-quals --no-mixed --no-discordant --dovetail --maxins 700].

Count matrix generation and sequencing depth normalization. The *Xenopus laevis* genome was subset into 1000 bp bins. Reads from processed bam files were then tallied according to bins to generate a genome-wide count matrix. Mitochondrial associated reads and bins which contained no reads across all samples were removed. Size factors were then estimated using DESeq2 v1.42.1 (Love et al., 2014) to generate sequence depth normalized bigwig files. Count matrices were also vst transformed in DESeq2 then used to generate the read fragment correlation plot. For other analyses, only genomic bins containing at least 17 reads across at least 2 samples were kept and replicates for each condition were averaged.

DNA Methylation analysis. To get methylated CpG proportions for each sample (**Fig 4A**), H2A.Z peaks were first identified with SEACR (v1.3) (Meers et al., 2019) using a cutoff of 0.025 by AUC with a stringent threshold. Individual CpG data was then extracted using Bismark with a cutoff of 5 reads and disregarding the first 9 bp of read 2 (due to adapter fill-in). Methylation proportions for H2A.Z samples were then calculated for CpGs overlapping with H2A.Z peaks. For H3, only regions outside of identified H2A.Z peaks were used to assess the CpG methylation status of general genomic background non-coincident with H2A.Z enriched areas. To generate H3-associated methylation 500 bp tiles for use in plotting (**Suppl Fig 9B-D**), methylation data was extracted with a specified cutoff of 1 read and disregarding the first 9 bp of read 2 then imported into a methylRawList object with a minimum read coverage of 2 and counted over 500 bp tiles with a 500 bp step size and a minimum of 2 CpG sites using methylKit v1.28.0 (Akalin et al., 2012).

Generation of plots. Genomic annotations for the top 20 % of filtered bins containing the most reads for each condition were generated and proportions plotted using ChIPseeker v1.38.0 (Yu et al., 2015) with reference gene annotations gathered from Xenbase (Fisher et al., 2023). Heat maps and plot profiles were created using deepTools v3.5.5 (Ramírez et al., 2016). For comparison of H3 methylation sites and H2A.Z, a signal matrix was first generated using the tiled H3 methylation bigwigs against all annotated *Xenopus laevis* genes, removing genes with no methylation data available. The resulting gene list was then used to plot corresponding H2A.Z signals.

in vitro **mRNA Synthesis**

DNA sequences of proteins of interest were cloned into pSP64T plasmids modified to include a Kozak sequence (GCCACC) upstream of the coding sequence and linearized. pSP64T (DM#111) was a gift from Douglas Melton (Addgene Plasmid# 15030). RNA production was carried out using the MEGAscript™ SP6 transcription kit (Invitrogen, Cat# AM1330) as per manufacturer's protocol, with the addition of 4.5 mM CleanCap® Reagent AG (TriLink, Cat# N-7113) and a reduction in GTP concentration down to 1.5 mM final.

Chromatinization in Egg Extract Assays

pAS696 containing a 19-mer array of Widom 601 DNA was a gift from Aaron Straight (Guse et al., 2011). 601 and HSat2 arrays were digested with XbaI and EcoRI or XbaI and BamHI, respectively, along with DraI and HaeII. DNA fragments containing the array sequence were then purified through a PEG precipitation titration, starting at 4.5 % of PEG (MW8000) and increasing in 0.5 % increments until 8 % (NaCl added to 0.5 M final concentration in the starting solution). Fragment containing fractions were then assessed via agarose gel and purified via phenol-chloroform extraction. Fragment ends were biotinylated with biotin-14-dATP (Jena Bioscience, Cat# NU-835-BIO14-S) using Klenow Fragment (3´→ 5´ exo-) (NEB Cat# M0212) following manufacturer's protocol. Biotinylated DNA was phenol-chloroform extracted and bound to M-280 Streptavidin Dynabeads™ (Invitrogen, Cat# 11206D) at 300 ng DNA per 1 µl of beads. DNA bead binding was carried out at room temperature for a minimum of 1 h shaking in the following solution: 1x DNA Bead Binding buffer (DBB) [750 mM NaCl, 50 mM Tris-HCl pH 8.0, 0.25 mM EDTA, 0.05 % Triton-X-100]; 2.5 % (w/v) polyvinyl alcohol; 750 mM NaCl. DNA beads were then washed 2x with DBB and 3x with sperm dilution buffer (SDB) [150 mM Sucrose, 10 mM HEPES-KOH pH 8.0, 1 mM $MgCl_2$, 100 mM KCl] and added to egg extract at a ratio of 4 µl DNA beads to 30 µl of egg extract. Experiments that did not use mRNA for exogenous protein expression also included 0.1 mg/ml cycloheximide dissolved in EtOH. $CaCl_2$ was then added to the extracts at a final concentration of 0.3 mM and incubated at 20 ºC for 1 h. Samples were then diluted 10-fold with SDB, and DNA beads were collected on a magnetic rack and washed 3x with SDB + 0.05 % Triton-X-100 before running on SDS-PAGE gel and assessed via western blot.

Western Blot Analysis

Samples were boiled in 1x SDS loading buffer [125 mM Tris-HCl pH 6.8, 0.01 % SDS, 25 % glycerol, 0.03 mg/ml bromo-phenol blue, 350 mM 2-mercaptoethanol] then run on either a 4-20 % SDS-PAGE gel (Bio-Rad, Cat# 4561096) or 3-8 % Tris-acetate gel (for SRCAP detection)

(Invitrogen, Cat# EA0375BOX). Samples were then transferred from the gel to a nitrocellulose membrane (Cytiva, 0.1 µm pore size, Cat# 10600000) overnight at 4 ºC in 1x transfer buffer [20 mM Tris, 150 mM Glycine, 20 % Methanol] (14V). Membranes were blocked for 30 min at RT with Intercept® (TBS) Protein-Free Blocking Buffer (LICORbio, Cat# 927-80001), followed by primary antibody incubation (diluted in Intercept® T20 (TBS) Antibody diluent (LICORbio, Cat# 927-65001)) for 1 h at RT. Membranes were then washed 3x, 5 min each wash, in 1xTBS+0.05 % Tween-20 then incubated with appropriate secondary antibodies for 1 h at RT and washed. Blots were then imaged on a LI-COR Odyssey M system and signals quantified using ImageJ via histogram analysis as previously described in (Stael et al., 2022). Ratios of either H2A.Z or H2A.X-F signals to H4 signals were then determined for normalization purposes in the chromatinization assays.

SRCAP Depletion from Egg Extract

SRCAP antibody was bound to Protein A Dynabeads™ (Invitrogen, Cat# 10008D) at a concentration of 0.8 µg antibody per 1 µl of beads overnight at 4 ºC in wash/coupling (W/C) buffer [10 mM HEPES-KOH pH 8.0, 150 mM NaCl]. Beads were then washed 2x with W/C buffer and 3x with SDB. An equal volume of beads and egg extract (supplemented with 0.1 mg/ml cycloheximide) were then incubated together for 1 h at 4 ºC and beads removed via magnet.

Other Instruments and Software Used

ÄKTA pure SN2626712 (Cytiva) and UNICORN v7.11 (Cytiva) for FPLC purification of histone proteins.
UCSF ChimeraX v1.9 (Meng et al., 2023) for structure visualization.
LI-COR Odyssey M, LI-COR Acquisition v1.2, and ImageJ v1.54f (Schneider et al., 2012) for western blot and gel imaging, data analysis, and visualization.
QuantStudio™ 5 (Thermo Fisher, Cat# A28574) and QuantStudio™ Design & Analysis v2.7 for QC of sequencing samples.
Inkscape v1.3.2 for figure generation.

DATA AVAILABILITY

Sequencing data can be accessed at GEO accension number GSE295057.

Raw data and analysis code can be accessed at Zenodo DOI: 10.5281/zenodo.15360677.

Cryo-EM maps and atomic models can be accessed with PDB IDs: 9OGS, 9OGZ (UM Sat2R-P); 9OGR, 9OH0 (Me Sat2R-P); 9OH1 (UM 601L); 9OH2 (Me 601L) and EMD IDs: EMD-70474 (UM Sat2R-P); EMD-70473 (Me Sat2R-P); EMD-70480 (UM 601L); EMD-70481 (Me 601L).

ACKNOWLEDGEMENTS

We thank Joanna Yeung, Justin Rendleman, Viviana Risca, and the rest of the Risca lab, as well as Richard Koche, for their invaluable advice and sharing of reagents for the sequencing and bioinformatics analysis. We thank members of the Funabiki lab for their continual advice, particularly Yiming Niu for Cryo-EM analysis help and Isabel Wassing for help in generating the α-H2A.Z antibody. We thank Dr. David Shechter for the XTC-2 cell line and α-H2A.X-F serums,

Shixin Liu and Aaron Straight for plasmids, and Tarun Kapoor for use of the Refeyn Two^{MP}. This work was conducted using the High-Performance Computing Resource Center, the Evelyn Gruss Lipper Cryo-Electron Microscopy Resource Center, and the Proteomics Resource Center at the Rockefeller University (with the help of Henrik Molina and Soeren Heissel for proteomics analysis). Animal husbandry was supported by the staff at the Rockefeller Comparative Bioscience Center.

AUTHOR CONTRIBUTIONS

R.M.S. and H.F. conceived and designed the study. R.M.S. and Y.A. designed and performed the Cryo-EM analysis. R.M.S. and H.A.K. designed physiological experiments. H.A.K. created the custom α-SRCAP antibody, prepared XTC-2 nuclei, and purified pG-Tn5. R.M.S. conducted all experiments and analysis. R.M.S. and H.F. prepared the manuscript with input from H.A.K. and Y.A.

FUNDING

This work was supported by the National Institutes of Health [R35GM132111] to H.F; the National Science Foundation Graduate Research Fellowship Program to R.M.S; Japan Society for the Promotion of Science Overseas Research Fellowships to H.A.K; and Osamu Hayaishi Memorial Scholarship for Study Abroad to Y.A..

CONFLICT OF INTEREST

H.F. is affiliated with the Graduate School of Medical Sciences, the Department of Biochemistry and Biophysics, Weill Cornell Medicine and the Cell Biology Program at the Sloan Kettering Institute. The authors declare no competing interests.

REFERENCES

Akalin A, Kormaksson M, Li S, Garrett-Bakelman FE, Figueroa ME, Melnick A, Mason CE. 2012. MethylKit: a comprehensive R package for the analysis of genome-wide DNA methylation profiles. *Genome Biol* **13**:1–9. doi:https://doi.org/10.1186/gb-2012-13-10-r87

Arimura Y, Konishi HA, Funabiki H. 2025. MagIC-Cryo-EM: Structural determination on magnetic beads for scarce macromolecules in heterogeneous samples. *Elife* **13**. doi:10.7554/ELIFE.103486.2

Arimura Y, Shih RM, Froom R, Funabiki H. 2021. Structural features of nucleosomes in interphase and metaphase chromosomes. *Mol Cell* **81**:4377. doi:10.1016/J.MOLCEL.2021.08.010

Belotserkovskaya R, Oh S, Bondarenko VA, Orphanides G, Studitsky VM, Reinberg D. 2003. FACT facilitates transcription-dependent nucleosome alteration. *Science* **301**:1090–1093. doi:10.1126/SCIENCE.1085703

Bepler T, Morin A, Rapp M, Brasch J, Shapiro L, Noble AJ, Berger B. 2019. Positive-unlabeled convolutional neural networks for particle picking in cryo-electron micrographs. *Nature Methods 2019 16:11* **16**:1153–1160. doi:10.1038/s41592-019-0575-8

Berta DG, Kuisma H, Välimäki N, Räisänen M, Jäntti M, Pasanen A, Karhu A, Kaukomaa J, Taira A, Cajuso T, Nieminen S, Penttinen RM, Ahonen S, Lehtonen R, Mehine M, Vahteristo P, Jalkanen J, Sahu B, Ravantti J, Mäkinen N, Rajamäki K, Palin K, Taipale J, Heikinheimo O, Bützow R, Kaasinen E, Aaltonen LA. 2021. Deficient H2A.Z deposition is associated with genesis of uterine leiomyoma. *Nature 2021 596:7872* **596**:398–403. doi:10.1038/s41586-021-03747-1

Bevington S, Boyes J. 2013. Transcription-coupled eviction of histones H2A/H2B governs V(D)J recombination. *EMBO Journal* **32**:1381–1392. doi:https://doi.org/10.1038/emboj.2013.42

Bintu L, Kopaczynska M, Hodges C, Lubkowska L, Kashlev M, Bustamante C. 2011. The elongation rate of RNA polymerase determines the fate of transcribed nucleosomes. *Nat Struct Mol Biol* **18**:1394–1399. doi:10.1038/NSMB.2164

Bönisch C, Hake SB. 2012. Histone H2A variants in nucleosomes and chromatin: More or less stable? *Nucleic Acids Res* **40**:10719–10741. doi:10.1093/nar/gks865

Buitrago D, Labrador M, Arcon JP, Lema R, Flores O, Esteve-Codina A, Blanc J, Villegas N, Bellido D, Gut M, Dans PD, Heath SC, Gut IG, Brun Heath I, Orozco M. 2021. Impact of DNA methylation on 3D genome structure. *Nature Communications 2021 12:1* **12**:1–17. doi:10.1038/s41467-021-23142-8

Buschbeck M, Hake SB. 2017. Variants of core histones and their roles in cell fate decisions, development and cancer. *Nat Rev Mol Cell Biol* **18**:299–314. doi:10.1038/nrm.2016.166

Chen P, Zhao J, Wang Y, Wang M, Long H, Liang D, Huang L, Wen Z, Li W, Li X, Feng H, Zhao H, Zhu P, Li M, Wang QF, Li G. 2013. H3.3 actively marks enhancers and primes gene transcription via opening higher-ordered chromatin. *Genes Dev* **27**:2109–2124. doi:10.1101/gad.222174.113

Chen Q, Yang R, Korolev N, Liu CF, Nordenskiöld L. 2017. Regulation of Nucleosome Stacking and Chromatin Compaction by the Histone H4 N-Terminal Tail–H2A Acidic Patch Interaction. *J Mol Biol* **429**:2075–2092. doi:10.1016/J.JMB.2017.03.016

Chen S. 2023. Ultrafast one-pass FASTQ data preprocessing, quality control, and deduplication using fastp. *iMeta* **2**:e107. doi:10.1002/IMT2.107

Choy JS, Wei S, Lee JY, Tan S, Chu S, Lee TH. 2010. DNA methylation increases nucleosome compaction and rigidity. *J Am Chem Soc* **132**:1782–1783. doi:https://doi.org/10.1021/ja910264z

Chua EYD, Vasudevan D, Davey GE, Wu B, Davey CA. 2012a. The mechanics behind DNA sequence-dependent properties of the nucleosome. *Nucleic Acids Res* **40**:6338–6352. doi:10.1093/NAR/GKS261

Chua EYD, Vasudevan D, Davey GE, Wu B, Davey CA. 2012b. The mechanics behind DNA sequence-dependent properties of the nucleosome. *Nucleic Acids Res* **40**:6338–6352. doi:10.1093/NAR/GKS261

Coleman-Derr D, Zilberman D. 2012. Deposition of Histone Variant H2A.Z within Gene Bodies Regulates Responsive Genes. *PLoS Genet* **8**:e1002988. doi:10.1371/journal.pgen.1002988

Colino-Sanguino Y, Clark SJ, Valdes-Mora F. 2022. The H2A.Z-nucleosome code in mammals: emerging functions. *Trends in Genetics* **38**:273–289. doi:10.1016/J.TIG.2021.10.003

Collings CK, Waddell PJ, Anderson JN. 2013. Effects of DNA methylation on nucleosome stability. *Nucleic Acids Res* **41**:2918–2931. doi:10.1093/NAR/GKS893

Conerly ML, Teves SS, Diolaiti D, Ulrich M, Eisenman RN, Henikoff S. 2010. Changes in H2A.Z occupancy and DNA methylation during B-cell lymphomagenesis. *Genome Res* **20**:1383–1390. doi:10.1101/gr.106542.110

Dai L, Xiao X, Pan L, Shi L, Xu N, Zhang Z, Feng X, Ma L, Dou S, Wang P, Zhu B, Li W, Zhou Z. 2021. Recognition of the inherently unstable H2A nucleosome by Swc2 is a major determinant for unidirectional H2A.Z exchange. *Cell Rep* **35**:109183. doi:10.1016/J.CELREP.2021.109183

Diegmüller F, Leers J, Hake SB. 2025. The “Ins and Outs and What-Abouts” of H2A.Z: A tribute to C. David Allis. *J Biol Chem* **301**. doi:10.1016/J.JBC.2025.108154

Dyer PN, Edayathumangalam RS, White CL, Bao Y, Chakravarthy S, Muthurajan UM, Luger K. 2003. Reconstitution of Nucleosome Core Particles from Recombinant Histones and DNA. *Methods Enzymol* **375**:23–44. doi:10.1016/S0076-6879(03)75002-2

Ehrlich M. 2003. The ICF syndrome, a DNA methyltransferase 3B deficiency and immunodeficiency disease. *Clinical Immunology* **109**:17–28. doi:10.1016/S1521-6616(03)00201-8

Emsley P, Lohkamp B, Scott WG, Cowtan K. 2010. Biological Crystallography Features and development of Coot. *Acta Crystallogr D Biol Crystallogr* **D66**:486–501. doi:10.1107/S0907444910007493

Engelke DR, Ng SY, Shastry BS, Roeder RG. 1980. Specific interaction of a purified transcription factor with an internal control region of 5S RNA genes. *Cell* **19**:717–728. doi:10.1016/S0092-8674(80)80048-1

Faast R, Thonglairoam V, Schulz TC, Beall J, Wells JRE, Taylor H, Matthaei K, Rathjen PD, Tremethick DJ, Lyons I. 2001. Histone variant H2A.Z is required for early mammalian development. *Current Biology* **11**:1183–1187. doi:10.1016/S0960-9822(01)00329-3

Fisher M, James-Zorn C, Ponferrada V, Bell AJ, Sundararaj N, Segerdell E, Chaturvedi P, Bayyari N, Chu S, Pells T, Lotay V, Agalakov S, Wang DZ, Arshinoff BI, Foley S, Karimi K, Vize PD, Zorn AM. 2023. Xenbase: key features and resources of the Xenopus model organism knowledgebase. *Genetics* **224**:18. doi:10.1093/GENETICS/IYAD018

Fujii Y, Wakamori M, Umehara T, Yokoyama S. 2016. Crystal structure of human nucleosome core particle containing enzymatically introduced CpG methylation. *FEBS Open Bio* **6**:498–514. doi:10.1002/2211-5463.12064

Giaimo BD, Ferrante F, Herchenröther A, Hake SB, Borggrefe T. 2019. The histone variant H2A.Z in gene regulation. *Epigenetics & Chromatin 2019 12:1* **12**:1–22. doi:10.1186/S13072-019-0274-9

Götzke H, Kilisch M, Martínez-Carranza M, Sograte-Idrissi S, Rajavel A, Schlichthaerle T, Engels N, Jungmann R, Stenmark P, Opazo F, Frey S. 2019. The ALFA-tag is a highly versatile tool for nanobody-based bioscience applications. *Nature Communications 2019 10:1* **10**:1–12. doi:10.1038/s41467-019-12301-7

Guse A, Carroll CW, Moree B, Fuller CJ, Straight AF. 2011. In vitro centromere and kinetochore assembly on defined chromatin templates. *Nature* **477**:354–358. doi:10.1038/NATURE10379

Hardy S, Jacques PÉ, Gévry N, Forest A, Fortin MÈ, Laflamme L, Gaudreau L, Robert F. 2009. The euchromatic and heterochromatic landscapes are shaped by antagonizing effects of transcription on H2A.Z deposition. *PLoS Genet* **5**:e1000687. doi:10.1371/JOURNAL.PGEN.1000687

Heo K, Kim H, Choi SH, Choi J, Kim K, Gu J, Lieber MR, Yang AS, An W. 2008. FACT-mediated exchange of histone variant H2AX regulated by phosphorylation of H2AX and ADP-ribosylation of Spt16. *Mol Cell* **30**:86–97. doi:10.1016/J.MOLCEL.2008.02.029

Hite RK, MacKinnon R. 2017. Structural Titration of Slo2.2, a Na+-Dependent K+ Channel. *Cell* **168**:390-399.e11. doi:10.1016/J.CELL.2016.12.030

Horikoshi N, Kujirai T, Sato K, Kimura H, Kurumizaka H. 2019. Structure-based design of an H2A.Z.1 mutant stabilizing a nucleosome in vitro and in vivo. *Biochem Biophys Res Commun* **515**:719–724. doi:10.1016/j.bbrc.2019.06.012

Horikoshi N, Sato K, Shimada K, Arimura Y, Osakabe A, Tachiwana H, Hayashi-Takanaka Y, Iwasaki W, Kagawa W, Harata M, Kimura H, Kurumizaka H. 2013. Structural polymorphism in the L1 loop regions of human H2A.Z.1 and H2A.Z.2. *Acta Crystallogr D Biol Crystallogr* **69**:2431–2439. doi:10.1107/S090744491302252X

Hsu CC, Shi J, Yuan C, Zhao D, Jiang S, Lyu J, Wang X, Li H, Wen H, Li W, Shi X. 2018a. Recognition of histone acetylation by the GAS41 YEATS domain promotes H2A.Z deposition in non-small cell lung cancer. *Genes Dev* **32**:58–69. doi:10.1101/GAD.303784.117/-/DC1

Hsu CC, Zhao D, Shi J, Peng D, Guan H, Li Y, Huang Y, Wen H, Li W, Li H, Shi X. 2018b. Gas41 links histone acetylation to H2A.Z deposition and maintenance of embryonic stem cell identity. *Cell Discov* **4**. doi:10.1038/S41421-018-0027-0

Ibarra-Morales D, Rauer M, Quarato P, Rabbani L, Zenk F, Schulte-Sasse M, Cardamone F, Gomez-Auli A, Cecere G, Iovino N. 2021. Histone variant H2A.Z regulates zygotic genome activation. *Nat Commun* **12**. doi:10.1038/S41467-021-27125-7

Ishibashi T, Dryhurst D, Rose KL, Shabanowitz J, Hunt DF, Ausió J. 2009. Acetylation of vertebrate H2A.Z and its effect on the structure of the nucleosome. *Biochemistry* **48**:5007–5017. doi:10.1021/bi900196c

Jackson K, Yu MC, Arakawa K, Fiala E, Youn B, Fiegl H, Müller-Holzner E, Widschwendter M, Ehrlich M. 2004. DNA hypomethylation is prevalent even in low-grade breast cancers. *Cancer Biol Ther* **3**:1225–1231. doi:10.4161/CBT.3.12.1222

Jenness C, Giunta S, Müller MM, Kimura H, Muir TW, Funabiki H. 2018. HELLS and CDCA7 comprise a bipartite nucleosome remodeling complex defective in ICF syndrome. *Proc Natl Acad Sci U S A* **115**:E876–E885. doi:10.1073/PNAS.1717509115

Jeronimo C, Watanabe S, Kaplan CD, Peterson CL, Robert F. 2015. The Histone Chaperones FACT and Spt6 Restrict H2A.Z from Intragenic Locations. *Mol Cell* **58**:1113–1123. doi:10.1016/J.MOLCEL.2015.03.030

Jimenez-Useche I, Nurse NP, Tian Y, Kansara BS, Shim D, Yuan C. 2014. DNA Methylation Effects on Tetra-Nucleosome Compaction and Aggregation. *Biophys J* **107**:1629–1636. doi:10.1016/J.BPJ.2014.05.055

Jimenez-Useche I, Yuan C. 2012. The Effect of DNA CpG Methylation on the Dynamic Conformation of a Nucleosome. *Biophys J* **103**:2502–2512. doi:10.1016/J.BPJ.2012.11.012

Katagiri C, Ohsumi K. 1994. Remodeling of sperm chromatin induced in egg extracts of amphibians . *Int J Dev Biol* **38**:209–216.

Kaya-Okur HS, Janssens DH, Henikoff JG, Ahmad K, Henikoff S. 2020. Efficient low-cost chromatin profiling with CUT&Tag. *Nature Protocols 2020 15:10* **15**:3264–3283. doi:10.1038/s41596-020-0373-x

King AD, Huang K, Rubbi L, Liu S, Wang CY, Wang Y, Pellegrini M, Fan G. 2016. Reversible Regulation of Promoter and Enhancer Histone Landscape by DNA Methylation in Mouse Embryonic Stem Cells. *Cell Rep* **17**:289–302. doi:10.1016/J.CELREP.2016.08.083

Kireeva ML, Walter W, Tchernajenko V, Bondarenko V, Kashlev M, Studitsky VM. 2002. Nucleosome remodeling induced by RNA polymerase II: loss of the H2A/H2B dimer during transcription. *Mol Cell* **9**:541–552. doi:10.1016/S1097-2765(02)00472-0

Krueger F, Andrews SR. 2011. Bismark: a flexible aligner and methylation caller for Bisulfite-Seq applications. *Bioinformatics* **27**:1571–1572. doi:10.1093/BIOINFORMATICS/BTR167

Kurumizaka H, Kujirai T, Takizawa Y. 2021. Contributions of Histone Variants in Nucleosome Structure and Function. *J Mol Biol* **433**:166678. doi:10.1016/J.JMB.2020.10.012

Langecker M, Ivankin A, Carson S, Kinney SRM, Simmel FC, Wanunu M. 2015. Nanopores suggest a negligible influence of CpG methylation on nucleosome packaging and stability. *Nano Lett* **15**:783–790. doi:10.1021/nl504522n

Lashgari A, Millau JF, Jacques PÉ, Gaudreau L. 2017. Global inhibition of transcription causes an increase in histone H2A.Z incorporation within gene bodies. *Nucleic Acids Res* **45**:12715–12722. doi:10.1093/NAR/GKX879

Laskey RA, Mills AD, Morris NR. 1977. Assembly of SV40 chromatin in a cell-free system from Xenopus eggs. *Cell* **10**:237–243. doi:10.1016/0092-8674(77)90217-3

Lee JY, Lee J, Yue H, Lee TH. 2015. Dynamics of Nucleosome Assembly and Effects of DNA Methylation. *Journal of Biological Chemistry* **290**:4291–4303. doi:10.1074/JBC.M114.619213

Lee JY, Lee TH. 2012. Effects of DNA methylation on the structure of nucleosomes. *J Am Chem Soc* **134**:173–175. doi:https://doi.org/10.1021/ja210273w

Lewis TS, Sokolova V, Jung H, Ng H, Tan D. 2021. Structural basis of chromatin regulation by histone variant H2A.Z. *Nucleic Acids Res*. doi:10.1093/nar/gkab907

Li R, Grimm SA, Wade PA. 2021. CUT&Tag-BS for simultaneous profiling of histone modification and DNA methylation with high efficiency and low cost. *Cell Reports Methods* **1**:100118. doi:10.1016/J.CRMETH.2021.100118

Li S, Peng Y, Landsman D, Panchenko AR. 2022a. DNA methylation cues in nucleosome geometry, stability and unwrapping. *Nucleic Acids Res* **50**:1864–1874. doi:10.1093/NAR/GKAC097

Li S, Peng Y, Panchenko AR. 2022b. DNA methylation: Precise modulation of chromatin structure and dynamics. *Curr Opin Struct Biol* **75**:102430. doi:10.1016/J.SBI.2022.102430

Li S, Wei T, Panchenko AR. 2023. Histone variant H2A.Z modulates nucleosome dynamics to promote DNA accessibility. *Nature Communications 2023 14:1* **14**:1–10. doi:10.1038/s41467-023-36465-5

Li Z, Kono H. 2016. Distinct Roles of Histone H3 and H2A Tails in Nucleosome Stability. *Scientific Reports 2016 6:1* **6**:1–12. doi:10.1038/srep31437

Liebschner D, Afonine P V., Baker ML, Bunkoczi G, Chen VB, Croll TI, Hintze B, Hung LW, Jain S, McCoy AJ, Moriarty NW, Oeffner RD, Poon BK, Prisant MG, Read RJ, Richardson JS, Richardson DC, Sammito MD, Sobolev O V., Stockwell DH, Terwilliger TC, Urzhumtsev AG, Videau LL, Williams CJ, Adams PD. 2019. Macromolecular structure determination using X-rays, neutrons and electrons: recent developments in Phenix. *urn:issn:2059-7983* **75**:861–877. doi:10.1107/S2059798319011471

Liu X, Li B, Gorovsky MA. 1996. Essential and nonessential histone H2A variants in Tetrahymena thermophila. *Mol Cell Biol* **16**:4305. doi:10.1128/MCB.16.8.4305

Lohka MI, Maller JL. 1985. Induction of nuclear envelope breakdown, chromosome condensation, and spindle formation in cell-free extracts. *Journal of Cell Biology* **101**:518–523. doi:10.1083/JCB.101.2.518

Louder RK, Park G, Ye Z, Cha JS, Gardner AM, Lei Q, Ranjan A, Höllmüller E, Stengel F, Pugh BF, Wu C. 2024. Molecular basis of global promoter sensing and nucleosome capture by the SWR1 chromatin remodeler. *Cell* **187**. doi:10.1016/J.CELL.2024.09.007

Love MI, Huber W, Anders S. 2014. Moderated estimation of fold change and dispersion for RNA-seq data with DESeq2. *Genome Biol* **15**:1–21. doi:https://doi.org/10.1186/s13059-014-0550-8

Lowary PT, Widom J. 1998. New DNA sequence rules for high affinity binding to histone octamer and sequence-directed nucleosome positioning. *J Mol Biol* **276**:19–42. doi:10.1006/jmbi.1997.1494

Luger K, Mäder AW, Richmond RK, Sargent DF, Richmond TJ. 1997. Crystal structure of the nucleosome core particle at 2.8 Å resolution. *Nature* **389**:251–260. doi:10.1038/38444

Mann M, Risley MS, Eckhardt RA, Kasinsky HE. 1982. Characterization of spermatid/sperm basic chromosomal proteins in the genus Xenopus (Anura, Pipidae). *J Exp Zool* **222**:173–186. doi:10.1002/JEZ.1402220209

Mao Z, Pan L, Wang W, Sun J, Shan S, Dong Q, Liang X, Dai L, Ding X, Chen S, Zhang Z, Zhu B, Zhou Z. 2014. Anp32e, a higher eukaryotic histone chaperone directs preferential recognition for H2A.Z. *Cell Research 2014 24:4* **24**:389–399. doi:10.1038/cr.2014.30

Meers MP, Tenenbaum D, Henikoff S. 2019. Peak calling by Sparse Enrichment Analysis for CUT&RUN chromatin profiling. *Epigenetics Chromatin* **12**:1–11. doi:10.1186/S13072-019-0287-4/FIGURES/6

Meng EC, Goddard TD, Pettersen EF, Couch GS, Pearson ZJ, Morris JH, Ferrin TE. 2023. UCSF ChimeraX: Tools for structure building and analysis. *Protein Science* **32**:e4792. doi:10.1002/PRO.4792

Murphy PJ, Wu SF, James CR, Wike CL, Cairns BR. 2018. Placeholder Nucleosomes Underlie Germline-to-Embryo DNA Methylation Reprogramming. *Cell* **172**:993-1006.e13. doi:10.1016/j.cell.2018.01.022

Newport J, Kirschner M. 1982. A Major Developmental Transition in Early Xenopus Embryos: I. Characterization and Timing of Cellular Changes at the Midblastula Stage **30**:675–686.

Ngo TTM, Yoo J, Dai Q, Zhang Q, He C, Aksimentiev A, Ha T. 2016. Effects of cytosine modifications on DNA flexibility and nucleosome mechanical stability. *Nat Commun* **7**:1–9. doi:10.1038/ncomms10813

Nie WF, Lei M, Zhang M, Tang K, Huang H, Zhang C, Miki D, Liu P, Yang Y, Wang X, Zhang Heng, Lang Z, Liu N, Xu X, Yelagandula R, Zhang Huiming, Wang Z, Chai X, Andreucci A, Yu JQ, Berger F, Lozano-Duran R, Zhu JK. 2019. Histone acetylation recruits the SWR1 complex to regulate active DNA demethylation in Arabidopsis. *Proc Natl Acad Sci U S A* **116**:16641–16650. doi:https://doi.org/10.1073/pnas.1906023116

Obri A, Ouararhni K, Papin C, Diebold ML, Padmanabhan K, Marek M, Stoll I, Roy L, Reilly PT, Mak TW, Dimitrov S, Romier C, Hamiche A. 2014. ANP32E is a histone chaperone that removes H2A.Z from chromatin. *Nature 2014 505:7485* **505**:648–653. doi:10.1038/nature12922

Oikawa M, Simeone A, Hormanseder E, Teperek M, Gaggioli V, O'Doherty A, Falk E, Sporniak M, D'Santos C, Franklin VNR, Kishore K, Bradshaw CR, Keane D, Freour T, David L, Grzybowski AT, Ruthenburg

AJ, Gurdon J, Jullien J. 2020. Epigenetic homogeneity in histone methylation underlies sperm programming for embryonic transcription. *Nat Commun* **11**. doi:10.1038/S41467-020-17238-W

Osakabe A, Adachi F, Arimura Y, Maehara K, Ohkawa Y, Kurumizaka H. 2015. Influence of DNA methylation on positioning and DNA flexibility of nucleosomes with pericentric satellite DNA. *Open Biol* **5**. doi:10.1098/RSOB.150128

Park G, Patel AB, Wu C, Louder RK. 2024. Structures of H2A.Z-associated human chromatin remodelers SRCAP and TIP60 reveal divergent mechanisms of chromatin engagement. *bioRxiv* 2024.07.30.605802. doi:10.1101/2024.07.30.605802

Park YJ, Dyer PN, Tremethick DJ, Luger K. 2004. A new fluorescence resonance energy transfer approach demonstrates that the histone variant H2AZ stabilizes the histone octamer within the nucleosome. *Journal of Biological Chemistry* **279**:24274–24282. doi:10.1074/jbc.M313152200

Pérez A, Castellazzi CL, Battistini F, Collinet K, Flores O, Deniz O, Ruiz ML, Torrents D, Eritja R, Soler-López M, Orozco M. 2012. Impact of methylation on the physical properties of DNA. *Biophys J* **102**:2140–2148. doi:10.1016/j.bpj.2012.03.056

Postow L, Ghenoiu C, Woo EM, Krutchinsky AN, Chait BT, Funabiki H. 2008. Ku80 removal from DNA through double strand break-induced ubiquitylation. *J Cell Biol* **182**:467–479. doi:10.1083/JCB.200802146

Pudney M, Varma MGR, Leake CJ. 1973. Establishment of a cell line (XTC-2) from the South African clawed toad,Xenopus laevis. *Experientia 1973 29:4* **29**:466–467. doi:10.1007/BF01926785

Ramírez F, Ryan DP, Grüning B, Bhardwaj V, Kilpert F, Richter AS, Heyne S, Dündar F, Manke T. 2016. deepTools2: a next generation web server for deep-sequencing data analysis. *Nucleic Acids Res* **44**:W160–W165. doi:10.1093/NAR/GKW257

Ranjan A, Nguyen VQ, Liu S, Wisniewski J, Kim JM, Tang X, Mizuguchi G, Elalaoui E, Nickels TJ, Jou V, English BP, Zheng Q, Luk E, Lavis LD, Lionnet T, Wu C. 2020. Live-cell single particle imaging reveals the role of RNA polymerase II in histone H2A.Z eviction. *Elife* **9**:e55667. doi:10.7554/eLife.55667

Richard F, Jethmalani Y, Janssens D, Luo W, Wang R, Wu Y, Zhou Z, Ma Y, Zhang W, Wang Z, Hua P. 2025. Benchmark of chromatin–protein interaction methods in haploid round spermatids. *Front Cell Dev Biol* **13**:1572405. doi:10.3389/FCELL.2025.1572405

Rudnizky S, Bavly A, Malik O, Pnueli L, Melamed P, Kaplan A. 2016. H2A.Z controls the stability and mobility of nucleosomes to regulate expression of the LH genes. *Nat Commun* **7**. doi:10.1038/ncomms12958

Ruhl DD, Jin J, Cai Y, Swanson S, Florens L, Washburn MP, Conaway RC, Conaway JW, Chrivia JC. 2006. Purification of a human SRCAP complex that remodels chromatin by incorporating the histone variant H2A.Z into nucleosomes. *Biochemistry* **45**:5671–5677. doi:https://doi.org/10.1021/bi060043d

Scacchetti A, Becker PB. 2021. Variation on a theme: Evolutionary strategies for H2A.Z exchange by SWR1-type remodelers. *Curr Opin Cell Biol* **70**:1–9. doi:10.1016/J.CEB.2020.10.014

Scheres SHW. 2012. RELION: Implementation of a Bayesian approach to cryo-EM structure determination. *J Struct Biol* **180**:519–530. doi:10.1016/J.JSB.2012.09.006

Schneider CA, Rasband WS, Eliceiri KW. 2012. NIH Image to ImageJ: 25 years of image analysis. *Nature Methods 2012 9:7* **9**:671–675. doi:10.1038/nmeth.2089

Shechter D, Chitta RK, Xiao A, Shabanowitz J, Hunt DF, Allis CD. 2009. A distinct H2A.X isoform is enriched in Xenopus laevis eggs and early embryos and is phosphorylated in the absence of a checkpoint. *Proc Natl Acad Sci U S A* **106**:749–754. doi:https://doi.org/10.1073/pnas.0812207106

Soroczynski J, Anderson LJ, Yeung JL, Rendleman JM, Oren DA, Konishi HA, Risca VI. 2024. OpenTn5: Open-Source Resource for Robust and Scalable Tn5 Transposase Purification and Characterization. *bioRxiv* 2024.07.11.602973. doi:10.1101/2024.07.11.602973

Stael S, Miller LP, Fernández-Fernández ÁD, Van Breusegem F. 2022. Detection of Damage-Activated Metacaspase Activity by Western Blot in Plants. *Methods in Molecular Biology* **2447**:127–137. doi:10.1007/978-1-0716-2079-3_11/FIGURES/1

Suto RK, Clarkson MJ, Tremethick DJ, Luger K. 2000. Crystal structure of a nucleosome core particle containing the variant histone H2A.Z. *Nat Struct Biol* **7**:1121–1124. doi:10.1038/81971

Talbert PB, Henikoff S. 2016. Histone variants on the move: substrates for chromatin dynamics. *Nature Reviews Molecular Cell Biology 2016 18:2* **18**:115–126. doi:10.1038/nrm.2016.148

Thambirajah AA, Dryhurst D, Ishibashi T, Li A, Maffey AH, Ausió J. 2006. H2A.Z stabilizes chromatin in a way that is dependent on core histone acetylation. *Journal of Biological Chemistry* **281**:20036–20044. doi:10.1074/jbc.M601975200

Tilman G, Arnoult N, Lenglez S, Van Beneden A, Loriot A, De Smet C, Decottignies A. 2012. Cancer-linked satellite 2 DNA hypomethylation does not regulate Sat2 non-coding RNA expression and is initiated by heat shock pathway activation. *Epigenetics* **7**:903–913. doi:10.4161/EPI.21107

Tramantano M, Sun L, Au C, Labuz D, Liu Z, Chou M, Shen C, Luk E. 2016. Constitutive turnover of histone H2A.Z at yeast promoters requires the preinitiation complex. *Elife* **5**. doi:10.7554/ELIFE.14243

Tutter A V., Walter JC. 2006. Chromosomal DNA replication in a soluble cell-free system derived from Xenopus eggs. *Methods Mol Biol* **322**:121–137. doi:10.1007/978-1-59745-000-3_9

Unoki M. 2021. Chromatin remodeling in replication-uncoupled maintenance DNA methylation and chromosome stability: Insights from ICF syndrome studies. *Genes to Cells* **26**:349–359. doi:10.1111/GTC.12850

Van Daal A, Elgin SCR. 1992. A Histone Variant, H2AvD, is Essential in Drosophila melanogaster. *Mol Biol Cell* **3**:593–602. doi:https://doi.org/10.1091/mbc.3.6.593

Veenstra GJC, Destrée OHJ, Wolffe AP. 1999. Translation of maternal TATA-binding protein mRNA potentiates basal but not activated transcription in Xenopus embryos at the midblastula transition. *Mol Cell Biol* **19**:7972–7982. doi:10.1128/MCB.19.12.7972

Ward WS, Coffey DS. 1991. DNA packaging and organization in mammalian spermatozoa: comparison with somatic cells. *Biol Reprod* **44**:569–574. doi:10.1095/BIOLREPROD44.4.569

Wassing IE, Nishiyama A, Shikimachi R, Jia Q, Kikuchi A, Hiruta M, Sugimura K, Hong X, Chiba Y, Peng J, Jenness C, Nakanishi M, Zhao L, Arita K, Funabiki H. 2024. CDCA7 is an evolutionarily conserved hemimethylated DNA sensor in eukaryotes. *Sci Adv* **10**:eadp5753. doi:10.1126/SCIADV.ADP5753

Watanabe S, Peterson C. 2010. The INO80 family of chromatin-remodeling enzymes: regulators of histone variant dynamics. *Cold Spring Harb Symp Quant Biol* **75**:35–42. doi:https://doi.org/10.1101/sqb.2010.75.063

Weber CM, Henikoff JG, Henikoff S. 2010. H2A.Z nucleosomes enriched over active genes are homotypic. *Nat Struct Mol Biol* **17**:1500–1507. doi:10.1038/nsmb.1926

Wong N, Lam WC, Lai PBS, Pang E, Lau WY, Johnson PJ. 2001. Hypomethylation of Chromosome 1 Heterochromatin DNA Correlates with q-Arm Copy Gain in Human Hepatocellular Carcinoma. *Am J Pathol* **159**:465. doi:10.1016/S0002-9440(10)61718-X

Wühr M, Freeman RM, Presler M, Horb ME, Peshkin L, Gygi SP, Kirschner MW. 2014a. Deep Proteomics of the Xenopus laevis Egg using an mRNA-Derived Reference Database. *Current Biology* **24**:1467–1475. doi:10.1016/J.CUB.2014.05.044

Wühr M, Freeman RM, Presler M, Horb ME, Peshkin L, Gygi SP, Kirschner MW. 2014b. Deep proteomics of the Xenopus laevis egg using an mRNA-derived reference database. *Curr Biol* **24**:1467–1475. doi:10.1016/J.CUB.2014.05.044

Wykes SM, Krawetz SA. 2003. The structural organization of sperm chromatin. *J Biol Chem* **278**:29471–29477. doi:10.1074/JBC.M304545200

Xue JZ, Woo EM, Postow L, Chait BT, Funabiki H. 2013. Chromatin-bound Xenopus Dppa2 shapes the nucleus by locally inhibiting microtubule assembly. *Dev Cell* **27**:47–59. doi:10.1016/J.DEVCEL.2013.08.002

Yang YJ, Dong HL, Qiang XW, Fu H, Zhou EC, Zhang C, Yin L, Chen XF, Jia FC, Dai L, Tan ZJ, Zhang XH. 2020. Cytosine Methylation Enhances DNA Condensation Revealed by Equilibrium Measurements Using Magnetic Tweezers. *J Am Chem Soc* **142**:9203–9209. doi:https://doi.org/10.1021/jacs.9b11957

Yu G, Wang LG, He QY. 2015. ChIPseeker: an R/Bioconductor package for ChIP peak annotation, comparison and visualization. *Bioinformatics* **31**:2382–2383. doi:10.1093/BIOINFORMATICS/BTV145

Zemach A, McDaniel IE, Silva P, Zilberman D. 2010. Genome-wide evolutionary analysis of eukaryotic DNA methylation. *Science (1979)* **328**:916–919. doi:https://doi.org/10.1126/science.1186366

Zhang H, Roberts DN, Cairns BR. 2005. Genome-wide dynamics of Htz1, a histone H2A variant that poises repressed/basal promoters for activation through histone loss. *Cell* **123**:219–231. doi:10.1016/j.cell.2005.08.036

Zheng SQ, Palovcak E, Armache JP, Verba KA, Cheng Y, Agard DA. 2017. MotionCor2: anisotropic correction of beam-induced motion for improved cryo-electron microscopy. *Nature Methods 2017 14:4* **14**:331–332. doi:10.1038/nmeth.4193

Zhou J, Lei X, Shafiq S, Zhang W, Li Q, Li K, Zhu J, Dong Z, He XJ, Sun Q. 2023. DDM1-mediated R-loop resolution and H2A.Z exclusion facilitates heterochromatin formation in Arabidopsis. *Sci Adv* **9**. doi:10.1126/SCIADV.ADG2699

Zierhut C, Jenness C, Kimura H, Funabiki H. 2014. Nucleosomal regulation of chromatin composition and nuclear assembly revealed by histone depletion. *Nat Struct Mol Biol* **21**:617–625. doi:10.1038/NSMB.2845

Zilberman D, Coleman-Derr D, Ballinger T, Henikoff S. 2008. Histone H2A.Z and DNA methylation are mutually antagonistic chromatin marks. *Nature* **456**:125–129. doi:10.1038/nature07324

Zlatanova J, Thakar A. 2008. H2A.Z: View from the Top. *Structure*. doi:10.1016/j.str.2007.12.008

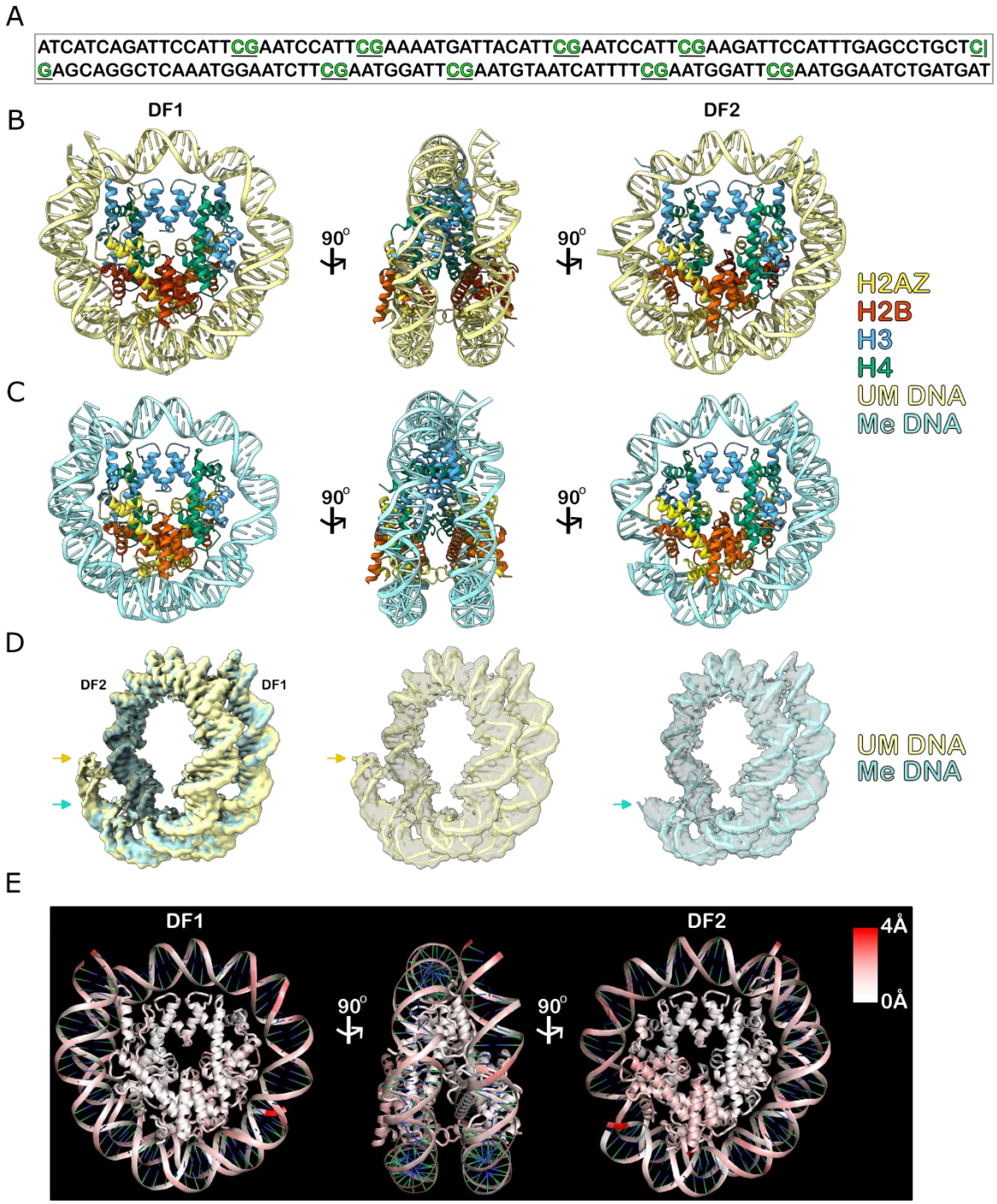

Figure 1. Cryo-EM structures of methylated and unmethylated Sat2R-P human H2A.Z nucleosomes. (A) Diagram of the palindromic Sat2R-P sequence. Methylated cytosines are labeled in green and underlined. Vertical bar denotes halfway point. **(B and C**) Atomic models of unmethylated (**B**) and methylated (**C**) Sat2R-P H2A.Z structures (the v1 model for both). Two face views (DF1 and DF2) and a side view (middle) are shown. **(D)** Left, overlay of unmethylated (UM) and methylated (Me) Sat2R-P DNA EM densities. Middle and right, overlays of DNA densities on top of the corresponding v1 DNA atomic models for either the unmethylated (middle) or methylated (right) structures. Arrows point to the visualizable end of the DF2 linker DNA for each structure. **(E)** RMSD analysis comparing differences between unmethylated and methylated v1 Sat2R-P H2A.Z atomic models.

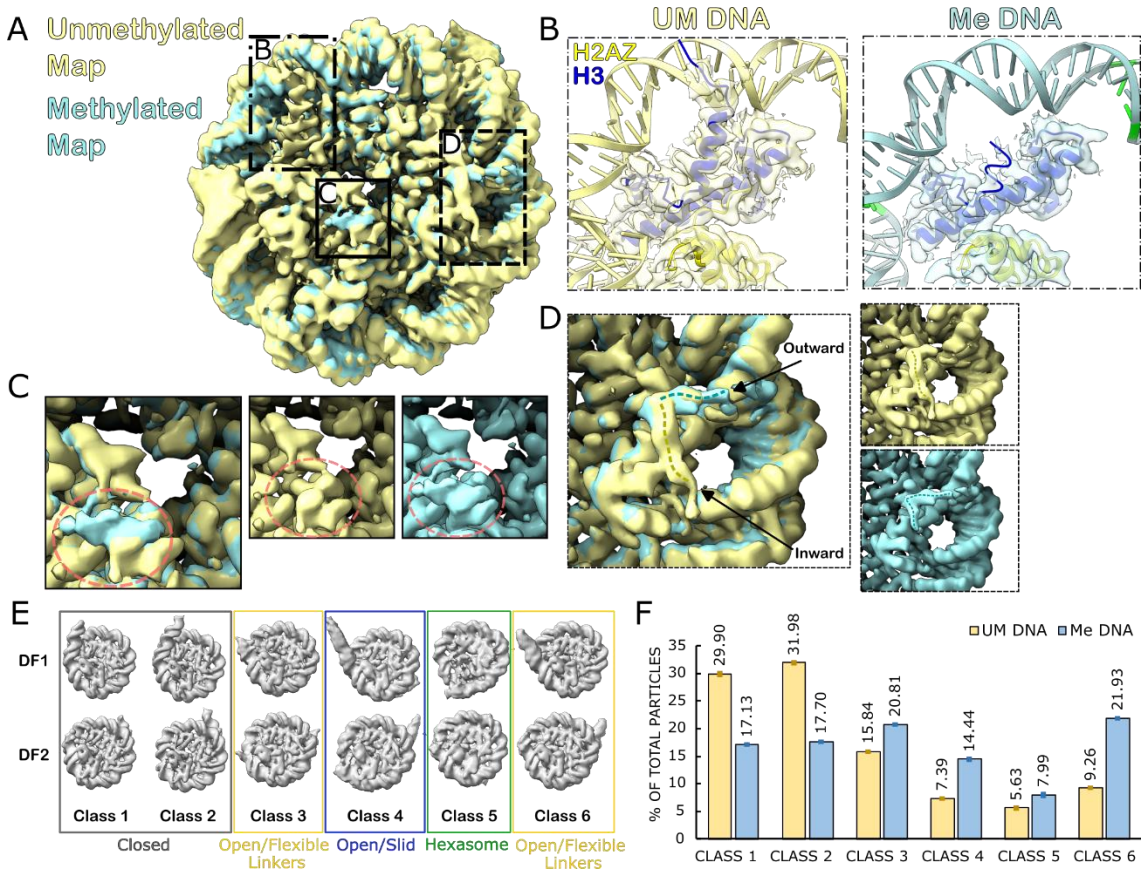

Figure 2. DNA methylation reduces H3-DNA contacts, alters H4 N-terminal tail orientations, and forms open nucleosome structures. (A) Density maps of unmethylated (UM) and methylated (Me) Sat2R-P H2A.Z nucleosomes filtered and resampled to ~3Å. The face shown, and all following zoom-ins, is of DF2. Maps are overlaid onto each other. Boxed regions highlight major areas of difference shown in **B-D**. **(B)** Zoom-in of the H3 N-terminus on DF2 of both structures. Density maps are shown as a transparent overlay on top of the corresponding v1 atomic models. **(C)** Zoom-in of the DF2 acidic patch on both structures. Area corresponding to the extra density found in the Me structure labeled in red. **(D)** Zoom-in of the H4 N-terminal tail. Dotted lines show each structure's preferred orientation **(E)** 3D Models used in the *in silico* mixing 3D classification analysis. Classes are as follows: (1 and 2) closed nucleosome structures with varying linker lengths; (3 and 6) open nucleosomes with highly flexible linkers; (4) open nucleosomes that have shifted position from center; (5) hexasomes. Both distal faces (DF1 and DF2) are shown of each model. **(F)** Results of classification analysis. Y-axis is the proportion of particles sorted into each class as a percent of the total input particles from each sample (UM or Me). Error bars represent SEM, n = 3 technical replicates.

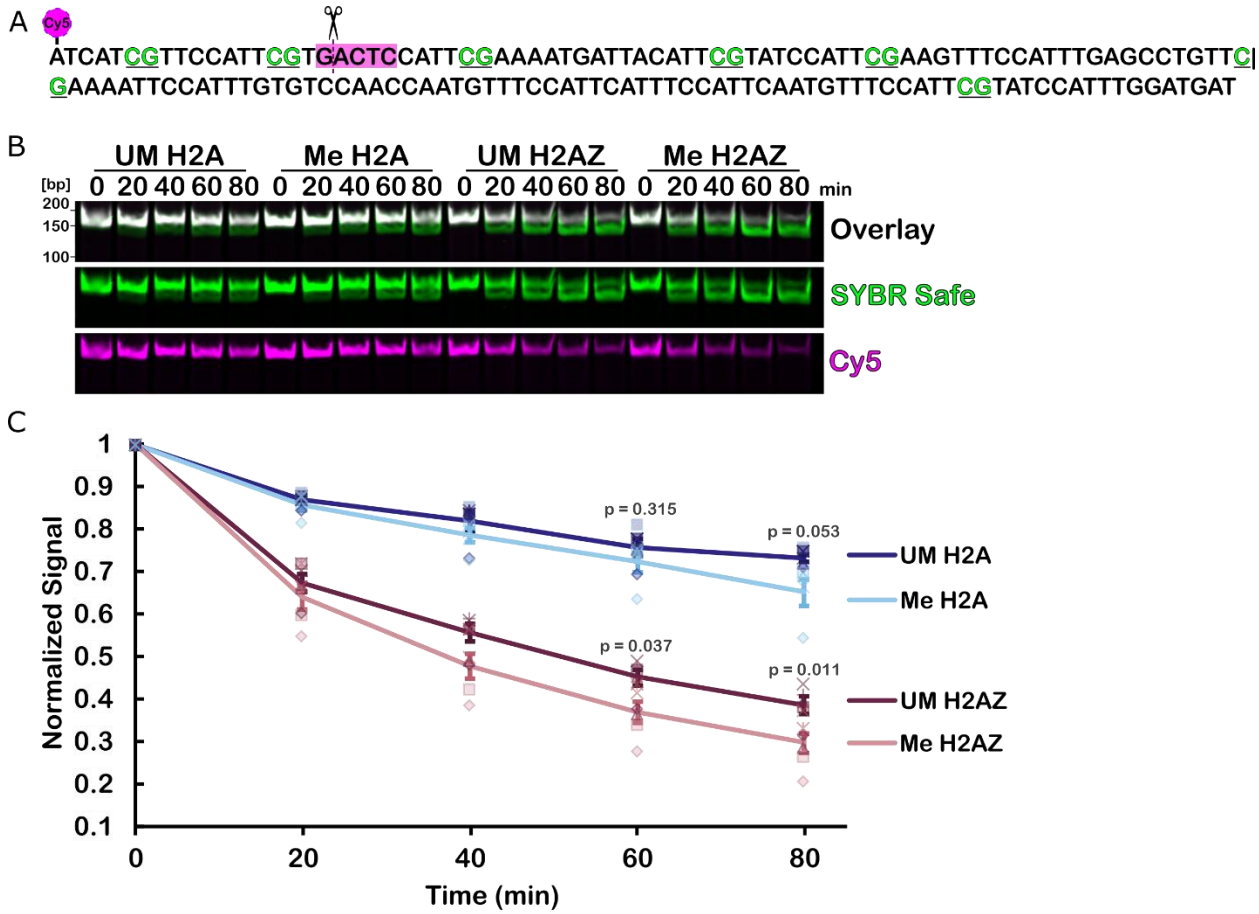

Figure 3. DNA methylation increases H2A.Z nucleosome accessibility. (A) Diagram of the 1HinfI_Sat2R DNA sequence used. CpG sites are shown in green and underlined. HinfI recognition site highlighted in magenta. A Cy5 fluorophore is attached to the 5′ end nearest the HinfI site. **(B)** Native gel showing HinfI digestion time course of UM and Me human H2A and H2A.Z nucleosomes. SYBR Safe was used to stain total DNA. Digestion efficiency was assessed via loss of Cy5 signal and a downward shift in the total DNA band. **(C)** Quantification of (**B**). Cy5 signals were normalized to total SYBR Safe signal for each sample. Error bars represent SEM. Each shape represents data from one independent experiment, n = 5 experiments. Statistics comparing unmethylated and methylated samples at indicated timepoints were completed with a two-tailed t-test assuming unequal variance with *p*-values listed above each comparison.

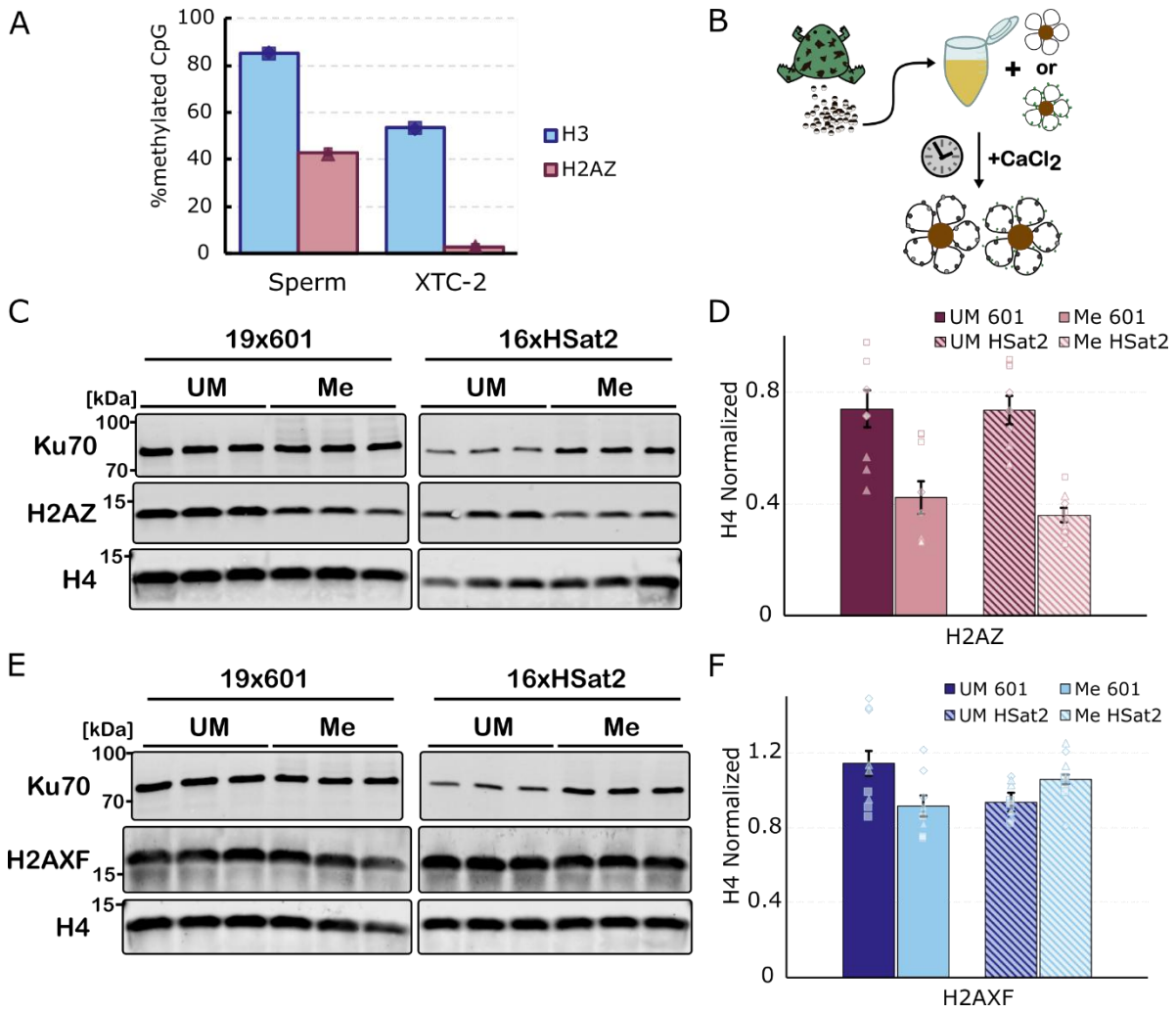

Figure 4. Presence or absence of DNA methylation influences H2A.Z deposition. (A) Percentage of methylated CpG sites (≥ 5x coverage) associated with H2A.Z peaks or H3 reads in sperm pronuclei incubated in interphase egg extract or XTC-2 nuclei following CnT-BS library preparation. H3 data is taken from regions outside of H2A.Z enriched peaks. Data points represent biological replicates (n = 2). **(B)** Schematic of chromatinization assay. Magnetic beads coated with DNA of interest were incubated in *Xenopus* egg extract with the addition of $CaCl_2$ to induce cycling into interphase. After 60 min, DNA beads were isolated to assess for histone composition. **(C and E)** Western blot results of chromatinization assay probing for either H2A.Z (**C**) or H2A.X-F (**E**). Ku70 and H4 signals are shown as loading controls. Beads coated with unmethylated (UM) or methylated (Me) 19-mer arrays of Widom 601 (19x601) or 16-mer arrays of HSat2 (16xHSat2) were used. A representative blot of technical triplicates for each condition is presented. **(D and F)** Quantification of (**C** and **E**). H2A.Z and H2A.X-F signals were normalized to H4 intensity. Error bars represent SEM. Data points represent technical triplicates across 3 biological replicates with each shape representing data from a single independent experiment (n = 9).

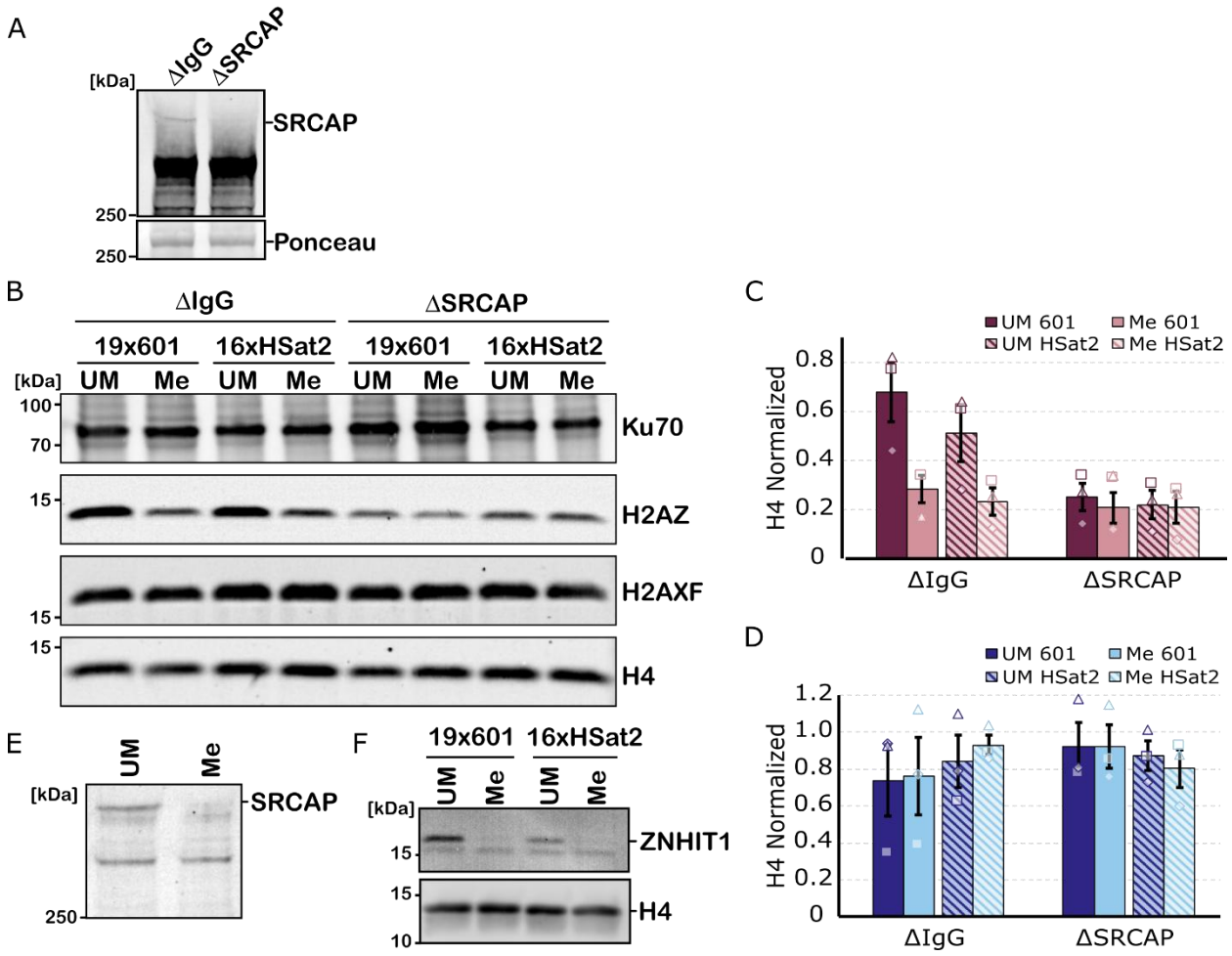

Figure 5. The SRCAP complex mediates H2A.Z's preferential association with unmethylated DNA. (A) Western blot to detect SRCAP in control IgG-depleted *Xenopus* egg extract (ΔIgG) or SRCAP-depleted extract (ΔSRCAP). Bottom panel shows ponceau staining as a loading control. **(B)** Western blots of chromatinization assay in IgG control vs SRCAP depleted egg extract. Magnetic beads coated with 19-mer arrays of Widom 601 (19x601) or 16-mer arrays of HSat2 (16xHSat2) were incubated with interphase egg extract for 60 min, before their isolation. **(C)** Quantification of H2A.Z signal normalized to H4 from **(B)**. **(D)** Quantification of H2A.X-F signal normalized to H4 from **(B)**. Error bars in (**C**) and (**D**) represent SEM from n = 3 biological replicates and each shape represents data from one independent experiment. **(E)** Western blot staining for SRCAP on 16xHSat2 DNA beads incubated in interphase egg extract. **(F)** Western blot staining for ZNHIT1 on specified DNA beads incubated in interphase egg extract. Representative image shown from two independent experiments.

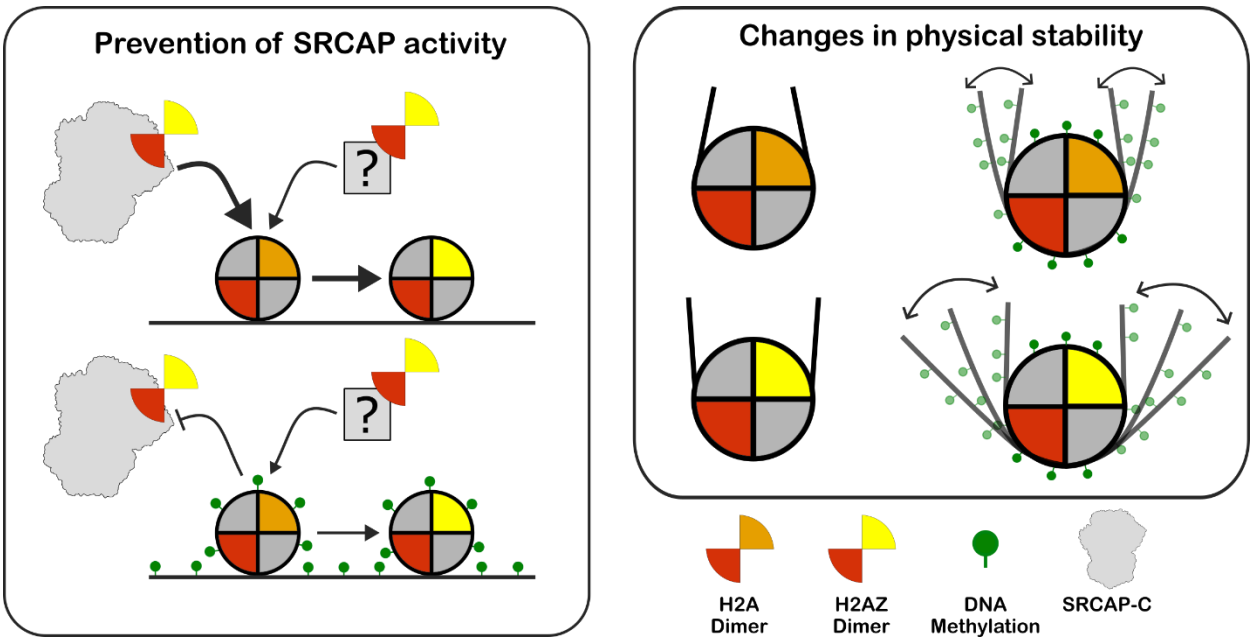

Figure 6. DNA methylation prevents SRCAP-C mediated H2A.Z deposition and creates more open and accessible H2A.Z nucleosome structures. Left, SRCAP-C is capable of depositing H2A.Z on unmethylated substrates, but presence of DNA methylation prevents binding and deposition activity. Another unidentified mechanism deposits H2A.Z in a DNA methylation insensitive manner. Right, DNA methylation decreases DNA wrapping stability, an effect felt greatest on the already open H2A.Z nucleosomes compared to the more tightly wrapped H2A nucleosomes, creating more open and accessible H2A.Z nucleosome structures.

Table 1. DNA sequences/oligos used in the study.							
Sequence Name	**Sequence**	**Vector**	**Plasmid Name**	**Insert Location**	**Source**	**Assay(s) Used In**	**Additional Notes**
Sat2R-P	ATCATCAGATTCCATTCGAATCCATTCGAAAATGATTACATTCGAATCCATTCGAAGATTCCATTTGAGCCTGCTCGAGCAGGCTCAAATGGAATCTTCGAATGGATTCGAATGTAATCATTTTCGAATGGATTCGAATGGAATCTGATGAT	pUC18	RMSp81	Between XbaI and BamHI sites	Generated and purchased from Integrated DNA Technologies (IDT™)	Cryo-EM	Modified from the Sat2R sequence in (Osakabe et al, 2015).
601L	ATCACAATCCCGGTGCCGAGGCCGCTCAATTGGTCGTAGACAGCTCTAGCACCGCTTAAACGCACGTACGGAATCCGTACGTGCGTTTAAGCGGTGCTAGAGCTGTCTACGACCAATTGAGCGGCCTCGGCACCGGGATTGTGAT	pUC57	601L-145-8X	EcoRV	(601L-145-8X) was a gift from Curt Davey (Addgene plasmid # 158572 ; http://n2t.net/addgene:158572 ; RRID:Addgene_158572)	Cryo-EM	
1HinfI_Sat2R	ATCATCGTTCCATTCGTGACTCCATTCGAAAATGATTACATTCGTATCCATTCGAAGTTTCCATTTGAGCCTGTTCGAAAATTCCATTTGTGTCCAACCAATGTTTCCATTCATTTCCATTCAATGTTTCCATTCGTATCCATTTGGATGAT	pUC18	RMSp161	Between XbaI and BamHI sites	Generated and purchased from Integrated DNA Technologies (IDT™)	Restriction Digest Assay	DNA generated via PCR amplification using following primers: /5Cy5/ATCATCGTTCCATTCGTGAC; ATCATCCAAATGGATACGAATGG
HSat2 arrays (1 repeat shown)	CGTTTGATTCCATTTGATGTTGATTCCATTCGAGTCCATTCGATGATAATTCCATTCGATTCTTTGCGATGATTCCATTCCTTTCCATTTGAGATGATTCCATTCGAGACCATTCGATGATTGCATTCAATTCATTCGATGACGATTATTCAATTCCGTTCAATGATTCCATTCGATTCCAATTGATGATGATTCCATTCGATTCCATTTGATGATGATTCCATGCGATTCCATTCGATGATGACTCCGATATCGGATCTGATATC	pUC18	RMSp64	Between XbaI and BamHI sites	Generated and purchased from Integrated DNA Technologies (IDT™)	Chromatinization Assays	GenBank: X06199.1
601 arrays (1 repeat shown)	CTGGAGAATCCCGGTGCCGAGGCCGCTCAATTGGTCGTAGCAAGCTCTAGCACCGCTTAAACGCACGTACGCGCTGTCCCCCGCGTTTTAACCGCCAAGGGGATTACTCCCTAGTCTCCAGGCACGTGTCAGATATATACATCCTGTGCATGTATTGAACAGCGACTCGGGTTATGTGATGGACCCTATACGCGGCCGCC	pUC18	pAS696	EcoRI/XbaI	Gift from Aaron Straight	Chromatinization Assays	
Oligos for Sequencing Library Preparation							
Sequence Name	**Sequence**				**Source**	**Assay(s) Used In**	**Additional Notes**
Tn5mC-Apt1	T/iMe-dC/GT/iMe-dC/GG/iMe-dC/AG/iMe-dC/GT/iMe-dC/AGATGTGTATAAGAGA/iMe-dC/AG				(Li et al, 2021); Generated and purchased from Integrated DNA Technologies (IDT™)	CnT-BS adapter oligo	Annealed with Tn5mC1.1-A1block to form adapter oligo
Tn5mC1.1-A1block	/5Phos/CTGTCTCTTATACA/3ddC/				(Li et al, 2021); Generated and purchased from Integrated DNA Technologies (IDT™)	CnT-BS adapter oligo	Annealed with Tn5mC-Apt1 to form adapter oligo
Tn5mC-ReplO1	/5Phos//iMe-dC/TGT/iMe-dC/T/iMe-dC/TTATA/iMe-dC/A/iMe-dC/AT/iMe-dC/T/iMe-dC//iMe-dC/GAG/iMe-dC//iMe-dC//iMe-dC/A/iMe-dC/GAGA/iMe-dC//3InvdT/				(Li et al, 2021); Generated and purchased from Integrated DNA Technologies (IDT™)	CnT-BS	Used during oligonucleotide replacement step

Table 2. Antibodies used in this study.						
Antigen	**Host**	**Company**	**Catalog No.**	**Peptide Used for Generation**	**Dilution**	**Assay(s) Used In**
H2A.Z	Rabbit	Custom		CIHKSLIGK KGQQKTV	2 µg/ml	Western Blots
H2A.Z	Rabbit	Active Motif	Cat#39013		1:10	CnT-BS
H3	Mouse	Cosmo Bio USA	MABI0001-100-EX		1:100	CnT-BS
H4	Mouse	Active Motif	Cat# 61521		1:1000	Western Blots
H2A.X-F	Rabbit	Custom, gift from David Shechter		Shechter et al. 2009	1:1000 (of serum)	Western Blots
Ku70	Rabbit	Custom		Postow et al. 2008	2 µg/ml	Western Blots
SRCAP	Rabbit	Custom		CPNSPSSH RVRKAKT	0.8 µg per 1 µl of beads (depletions); 12 µg/ml (WB)	Depletions; Western Blots
ZNHIT1	Rabbit	Proteintech	16595-1-AP		1:1000	Western Blots
P400	Rabbit	Bethyl	A300-541A		1:1000	Western Blots
ALFA tag	Alpaca (single domain antibody purified from E. coli)	NanoTag Biotechnologies	N1502-Li800-L		1:1000	Western Blots
Secondaries						
IRDye® 800CW anti-Rabbit IgG	Goat	LICORbio	926-32211		1:10000	Western Blots
IRDye® 680RD anti-Mouse IgG	Goat	LICORbio	926-68070		1:10000	Western Blots
anti-Rabbit IgG	Guinea Pig	antibodies-online.com	ABIN101961		1:100	CnT-BS
anti-Mouse IgG	Rabbit	abcam	ab46540		1:100	CnT-BS

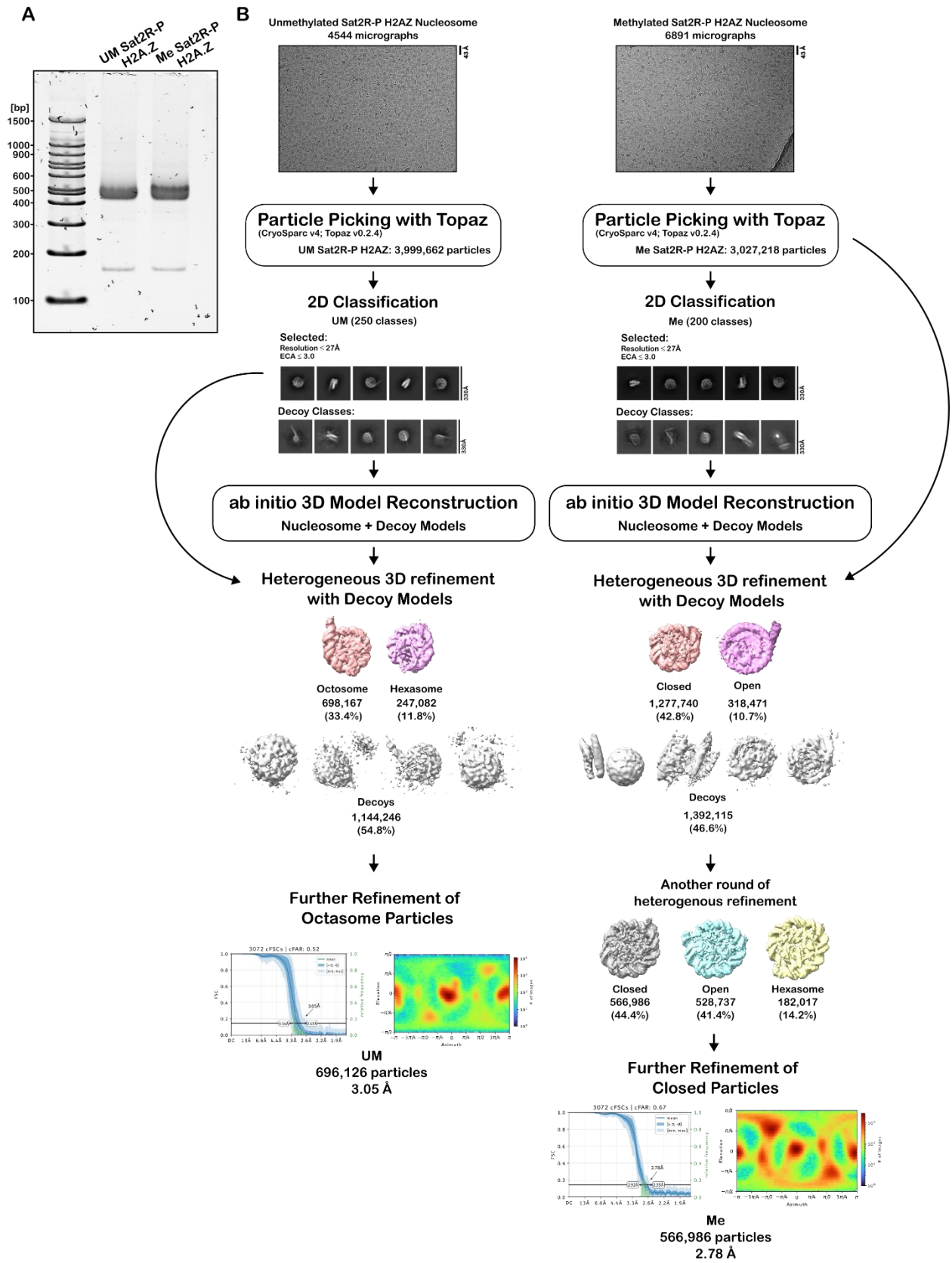

Supplementary Figure 1. Workflow of Sat2R-P cryo-EM analysis. (A) Native PAGE analysis of H2A.Z nucleosomes used for cryo-EM analysis. Bands visualized through SYBR Safe staining. **(B)** Diagram of structure analysis pipeline for either unmethylated (left) or methylated (right) H2A.Z SAT2R-P samples. Further details described in methods.

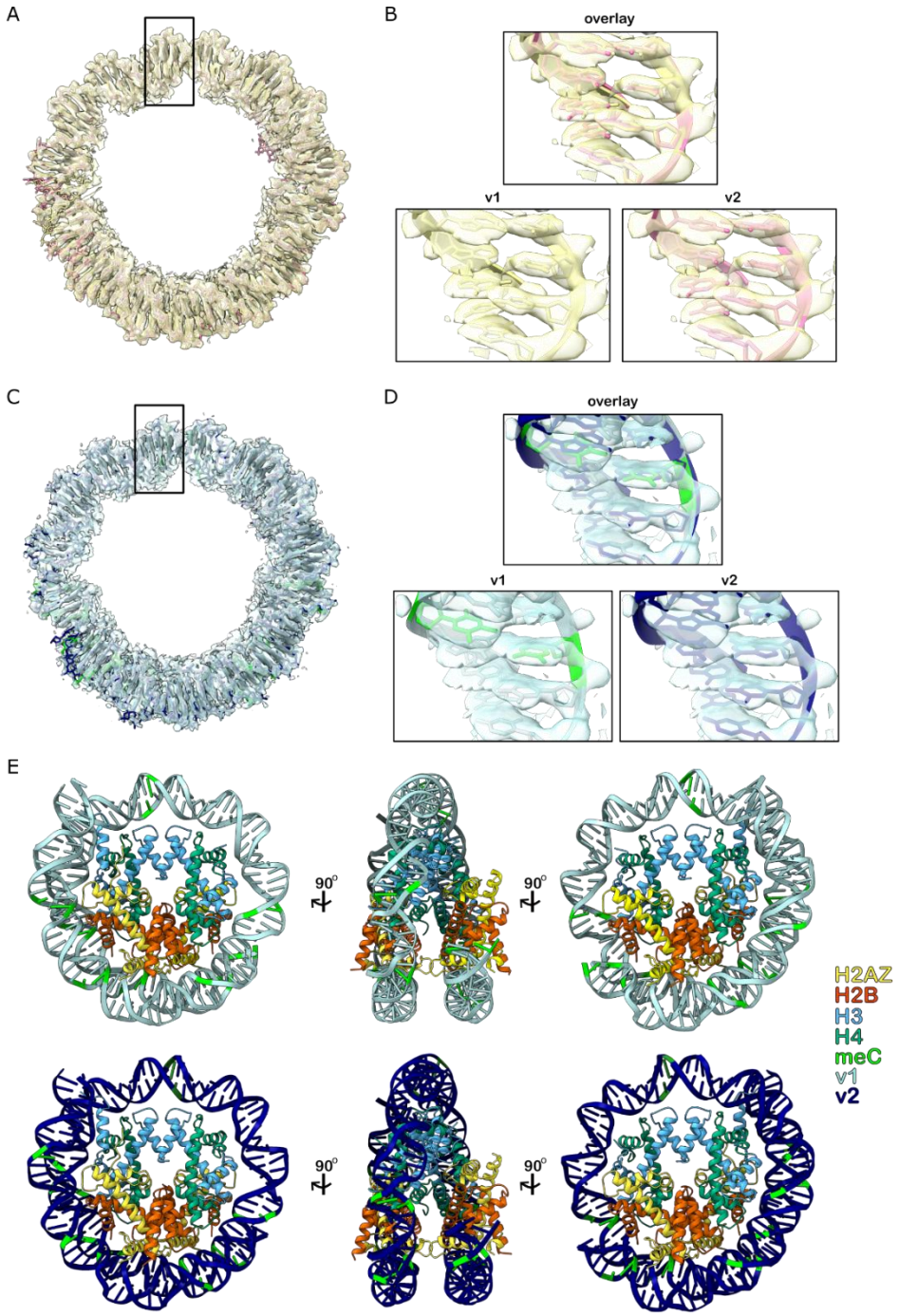

Supplementary Figure 2. DNA atomic model generation for Sat2R-P H2A.Z nucleosome structures. (A and C) Overlays of electron density maps for the DNA with both generated atomic models for either the unmethylated **(A)** or methylated **(C)** Sat2R-P H2A.Z nucleosome structure. **(B and D)** Zoom-in of dyad regions showing fitting of both DNA atomic models (v1 and v2) generated for either the unmethylated **(B)** or methylated **(D)** structure. Methylated cytosines are highlighted in green. Top panels are overlays of both models for the two structures. Positioning was determined by assessing densities around bases which retain purine/pyrimidine identity in both models vs those that switch. Bases that switched from purine to pyrimidine, and vice versa, showed more ambiguous densities than those that retained identity. Positioning was determined using the unmethylated structure and then used in modeling the methylated structure. (**E**) Comparison of predicted CpG positioning for the v1 (top) and v2 (bottom) atomic models generated for the methylated structure.

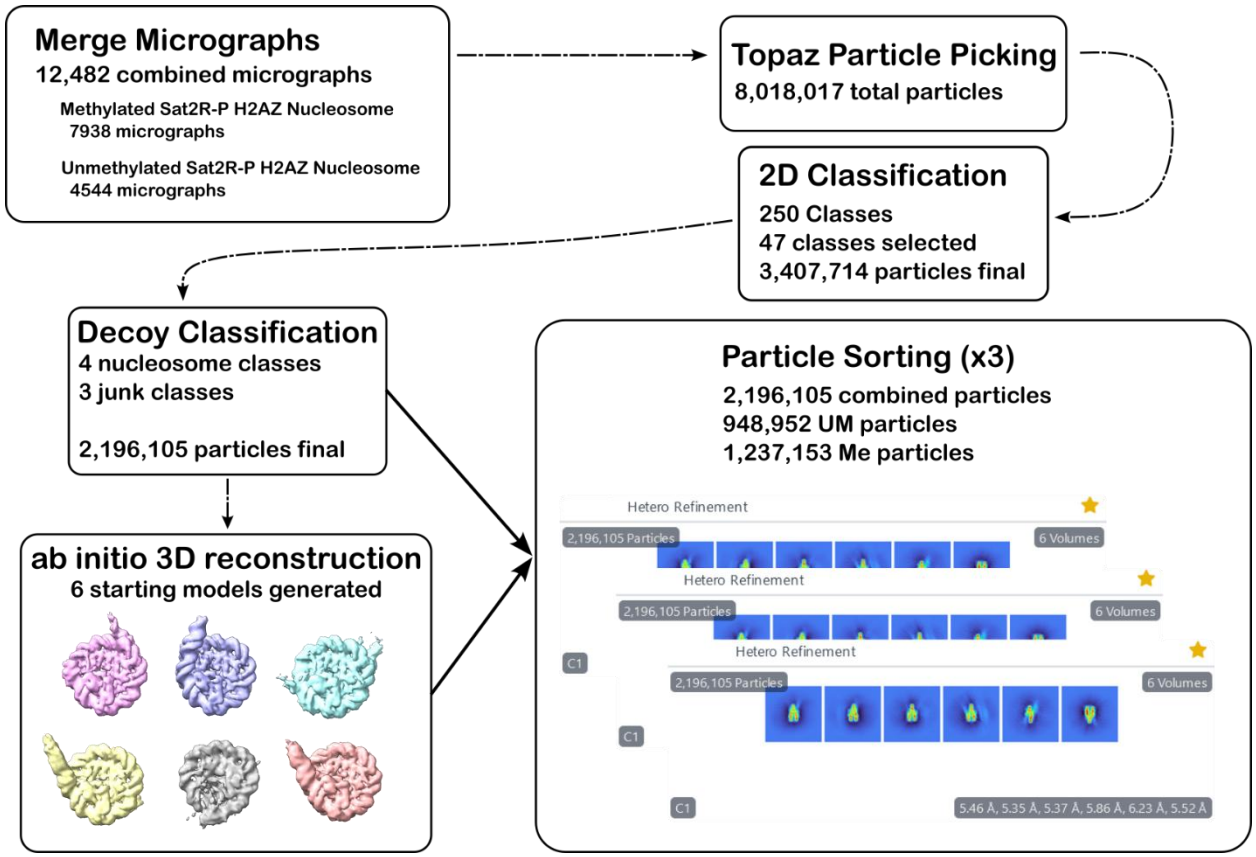

Supplementary Figure 3. Workflow of *in silico* mixing 3D classification analysis. Particles from a merged batch of unmethylated and methylated Sat2R-P H2A.Z nucleosome micrographs were picked and fed through the standard analysis pipeline. Six 3D models were then generated representing various open, closed, or hexasome-containing states of the nucleosome. Merged particles were then sorted to each of the classes through CryoSPARC's heterorefinement tool (n = 3 technical replicates).

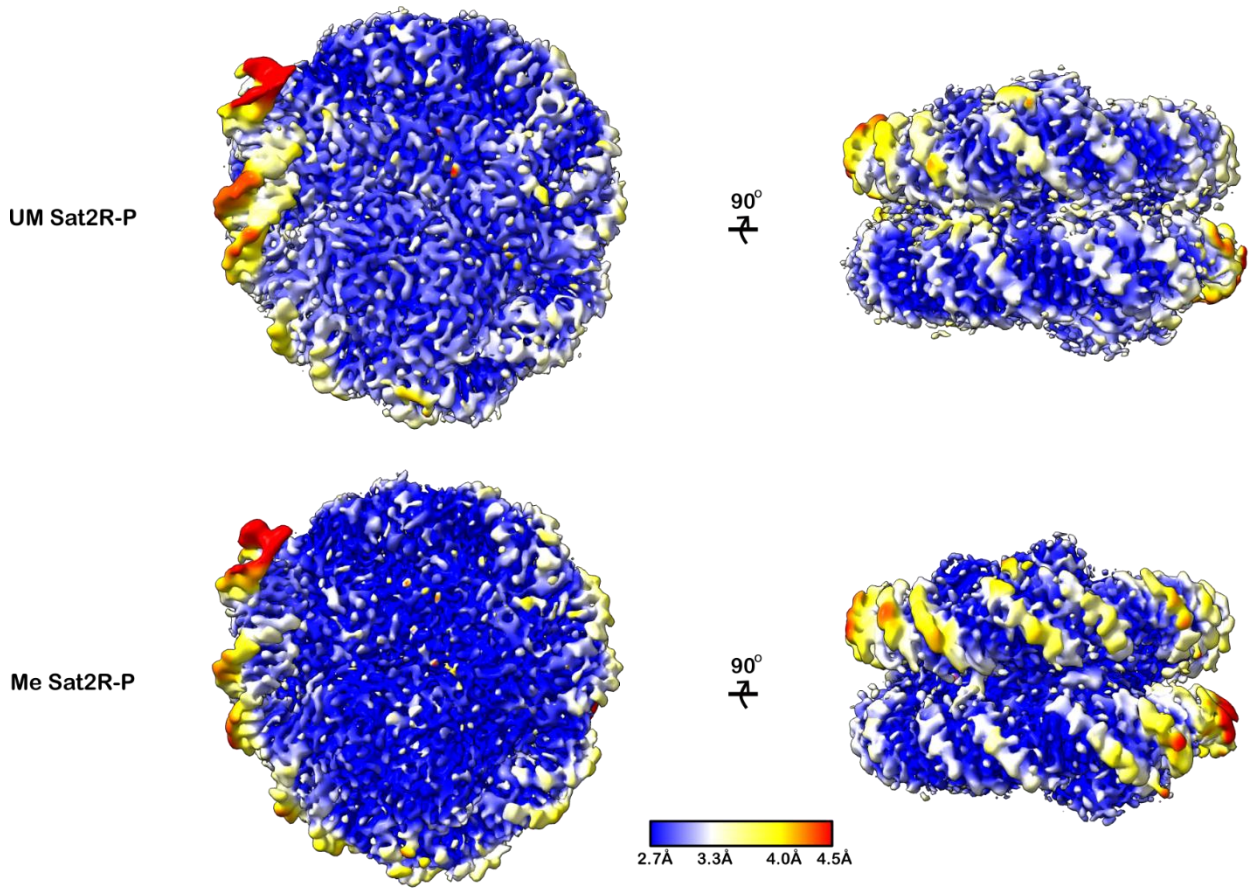

Supplementary Figure 4. Local resolution estimates for unmethylated and methylated Sat2R-P H2A.Z structures. Left, local resolution estimates of DF1 for both unmethylated (top) and methylated (bottom) Sat2R-P density maps. Right, side view showing local resolution of the DNA backbone for both methylated and unmethylated density maps. Local resolution maps were generated in CryoSPARC using the local resolution estimation tool and overlaid on density maps filtered using CryoSPARC's local filtering tool.

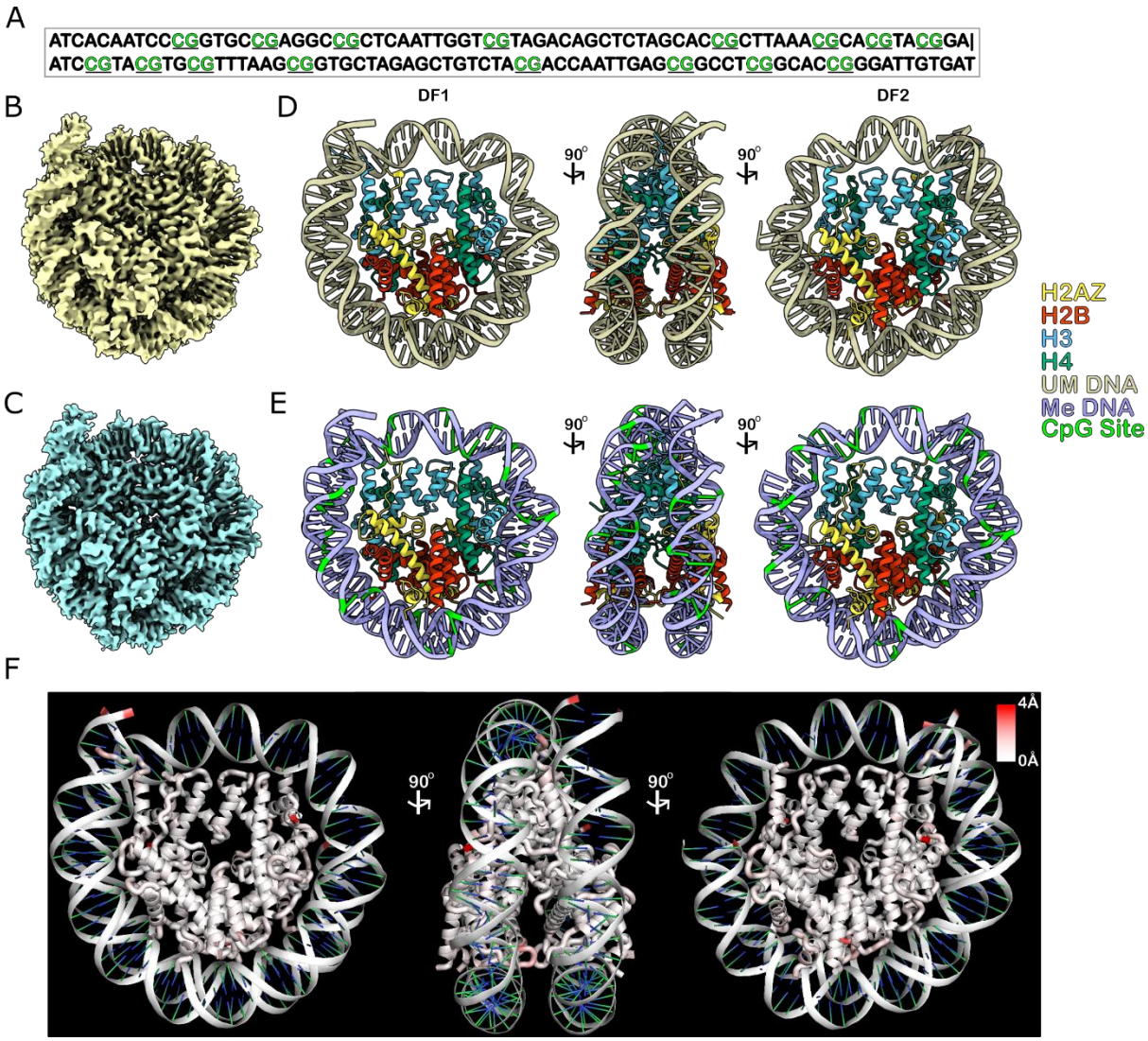

Supplementary Figure 5. Cryo-EM structures of 601L H2A.Z nucleosomes show no DNA methylation dependent differences. (A) Diagram of the palindromic 601L sequence. Bar indicates halfway point. Methylated cytosines are in green and underlined. **(B and C)** Final density maps of unmethylated **(B)** or methylated **(C)** H2A.Z nucleosomes. **(D and E)** Atomic models generated for **(B and C)**. Methylated cytosines shown in green **(F)** RMSD analysis comparing differences between methylated and unmethylated 601L H2A.Z atomic models.

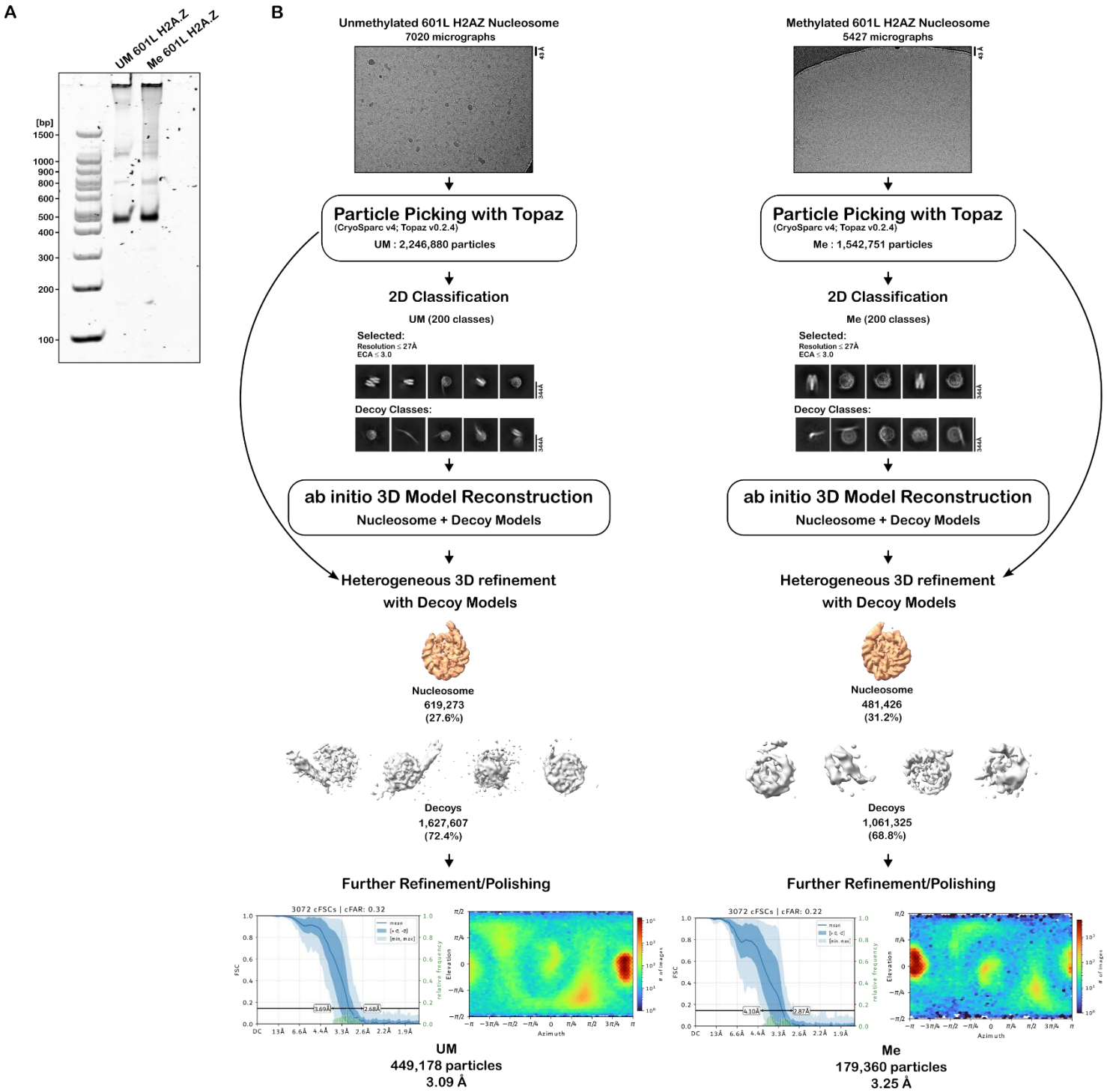

Supplementary Figure 6. Workflow of 601L H2A.Z nucleosome cryo-EM structures. (A) Native PAGE analysis of 601L H2A.Z nucleosome samples used for cryo-EM. Bands visualized through SYBR Safe staining. **(B)** Diagram showing analysis pipeline for solving 601L nucleosome structures. Further details described in methods.

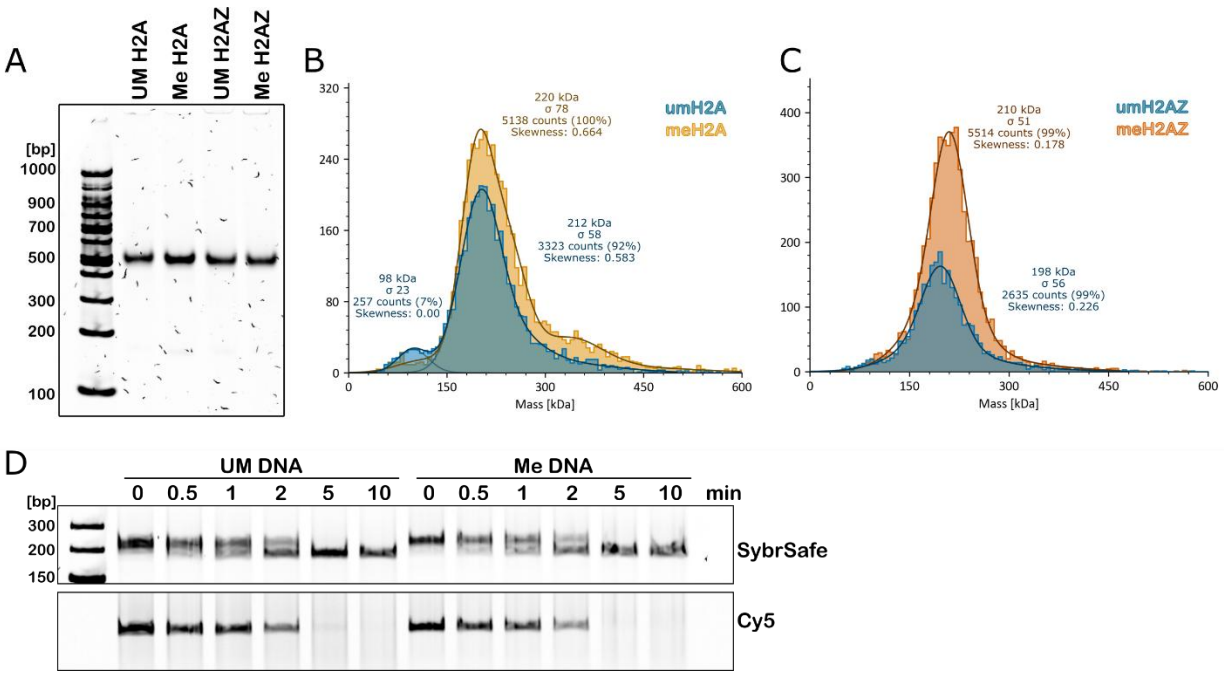

Supplementary Figure 7. Native PAGE and mass photometry analysis of nucleosomes used in HinfI digest assays. (A) Native PAGE analysis of nucleosome samples. Bands visualized through SYBR Safe staining. **(B and C)** Mass photometry analysis of methylated or unmethylated H2A **(B)** or H2A.Z **(C)** nucleosomes. Peaks around 200-220 kDa represent the fully formed nucleosome population. **(D)** HinfI digest time course of bare unmethylated or methylated DNA.

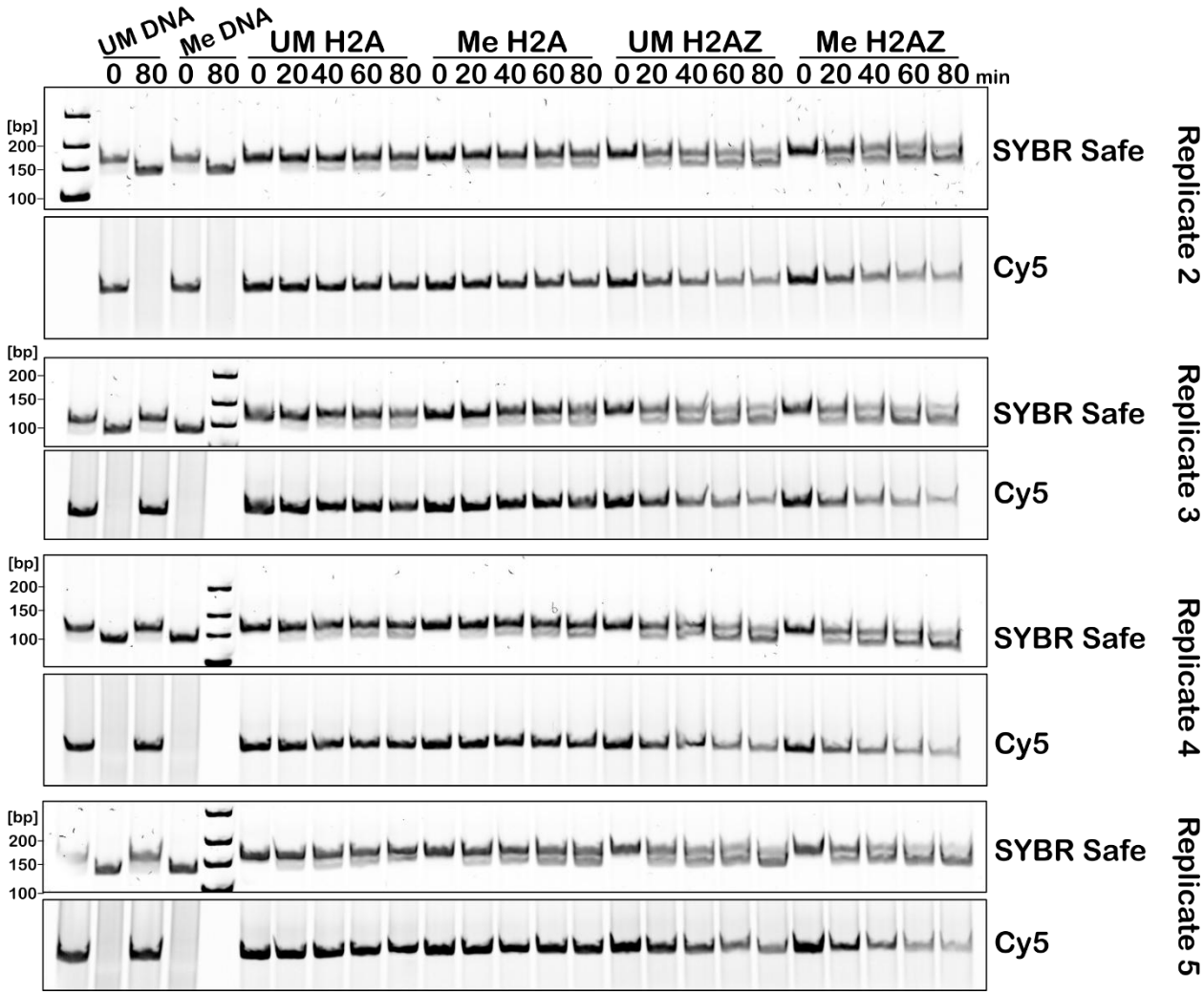

Supplementary Figure 8. Replicate gels of data from Main Figure 3.

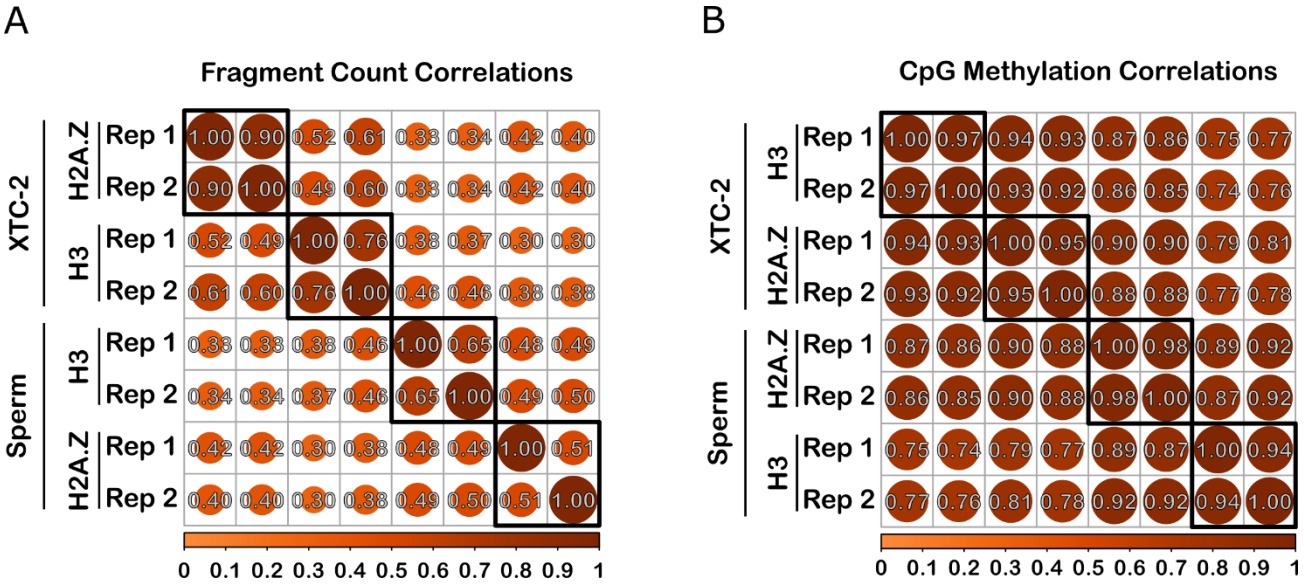

Supplementary Figure 9. Reproducibility comparison of CnT-BS samples (A) Pearson correlation plot comparing fragment counts mapped to 1000 bp genomic bins across samples. Bins containing zero fragments were first filtered out. Fragment counts were then normalized using DESeq2 to account for sequencing depth differences and underwent a variance stabilizing transformation (VST) before the correlation matrix was generated. **(C)** Pearson correlation plot comparing CpG methylation across samples. Percent methylation at individual CpG sites was calculated for high coverage CpGs (≥ 10 reads) and normalized using methylKit. The correlation matrix was then generated using pairwise observations across all eight samples. Both correlation matrices were ordered, and rectangles drawn (n = 4, user-specified), via hierarchical clustering.

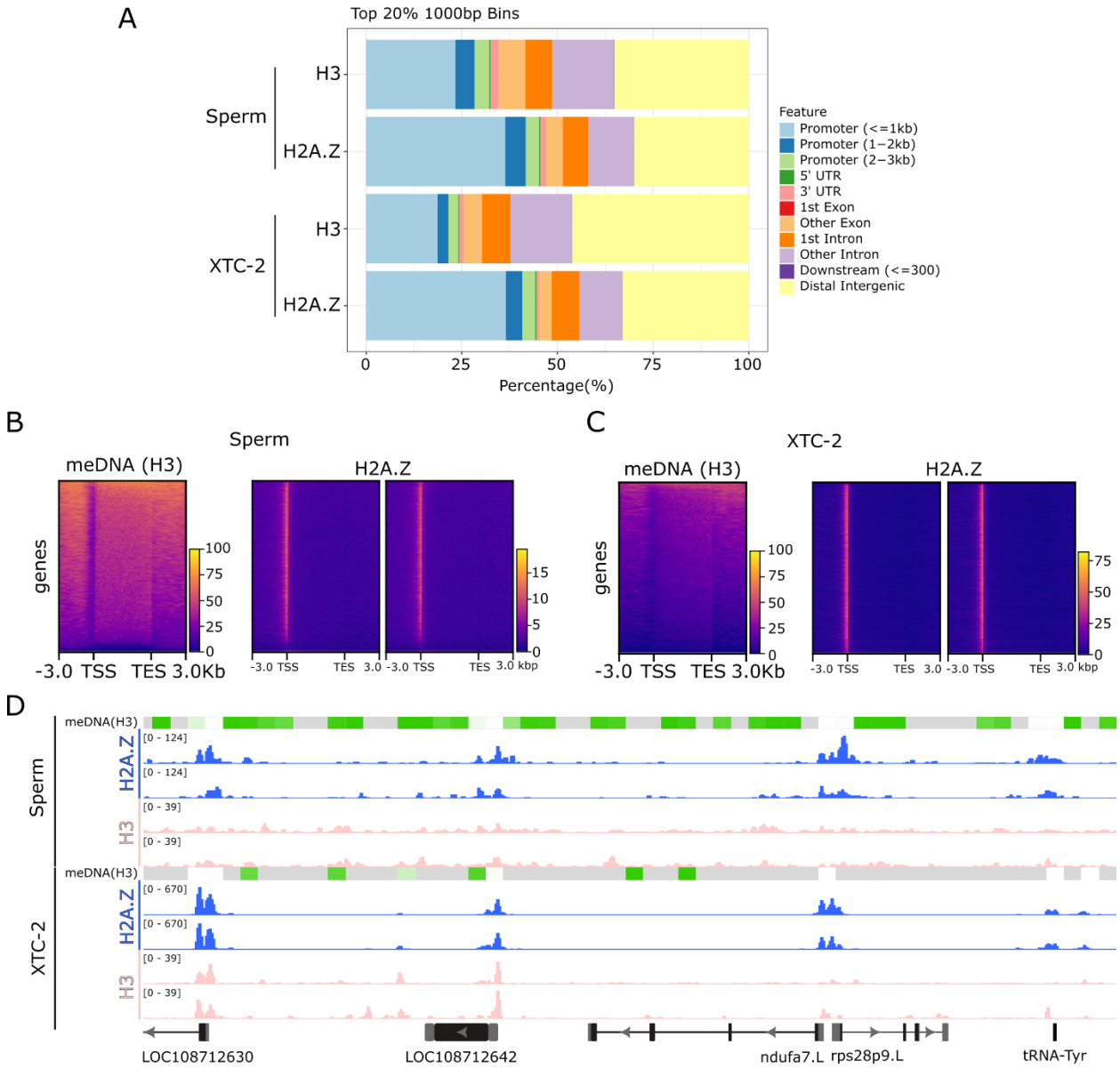

Supplementary Figure 10. H2A.Z localizes to hypomethylated TSSs. (A) Genomic annotation plots for the top quantile of 1000 bp genomic bins containing the most mapped reads averaged between replicates for each specified condition. **(B and C)** Heatmaps of either H3 CpG methylation calls averaged over 500 bp tiles (left-most panel) or H2A.Z reads (right panels) from two biological replicates across a representation of all annotated *Xenopus laevis* genes from either sperm (**B**) or XTC-2 (**C**) samples. Corresponding H3 and H2A.Z data are shown on the same sets of genes sorted in the same order. **(D)** IGV snapshot of a region on chromosome 1L showcasing preferential H2A.Z deposition at hypomethylated TSSs. Average H3 methylation tracks were generated across 500 bp tiles for visualization purposes on a scale of 0 to 100% CpG methylation. Grey indicates regions with no methylation data availability. Two biological replicates of H2A.Z and H3 tracks are shown.

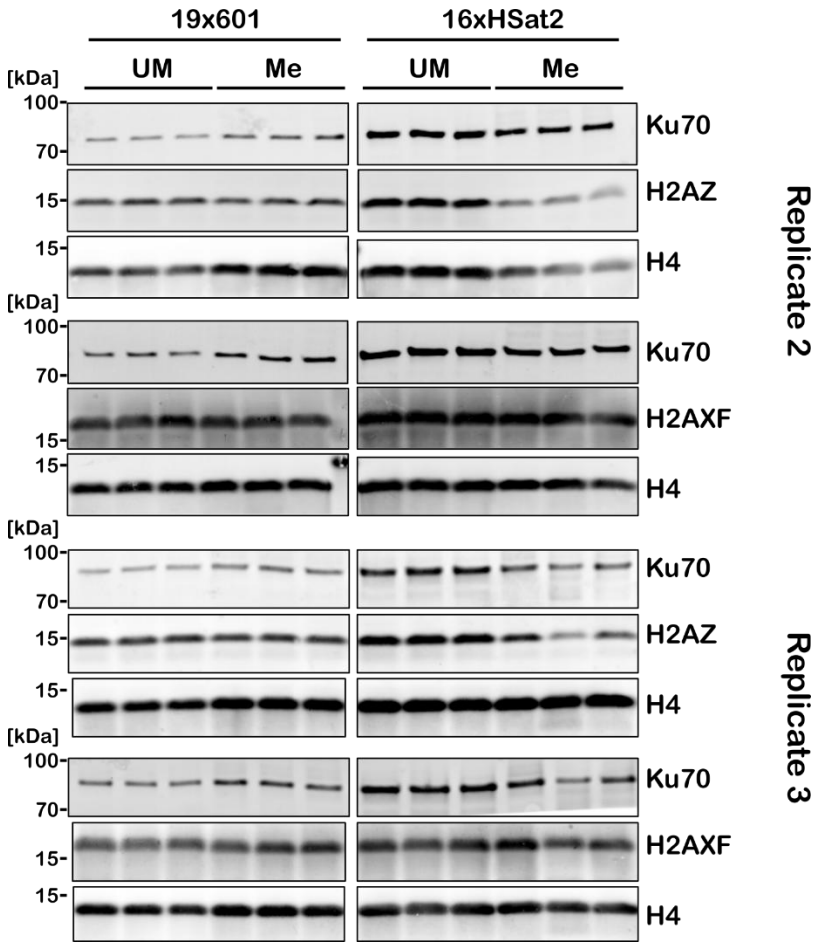

Supplementary Figure 11. Replicates of data from Main Figure 4.

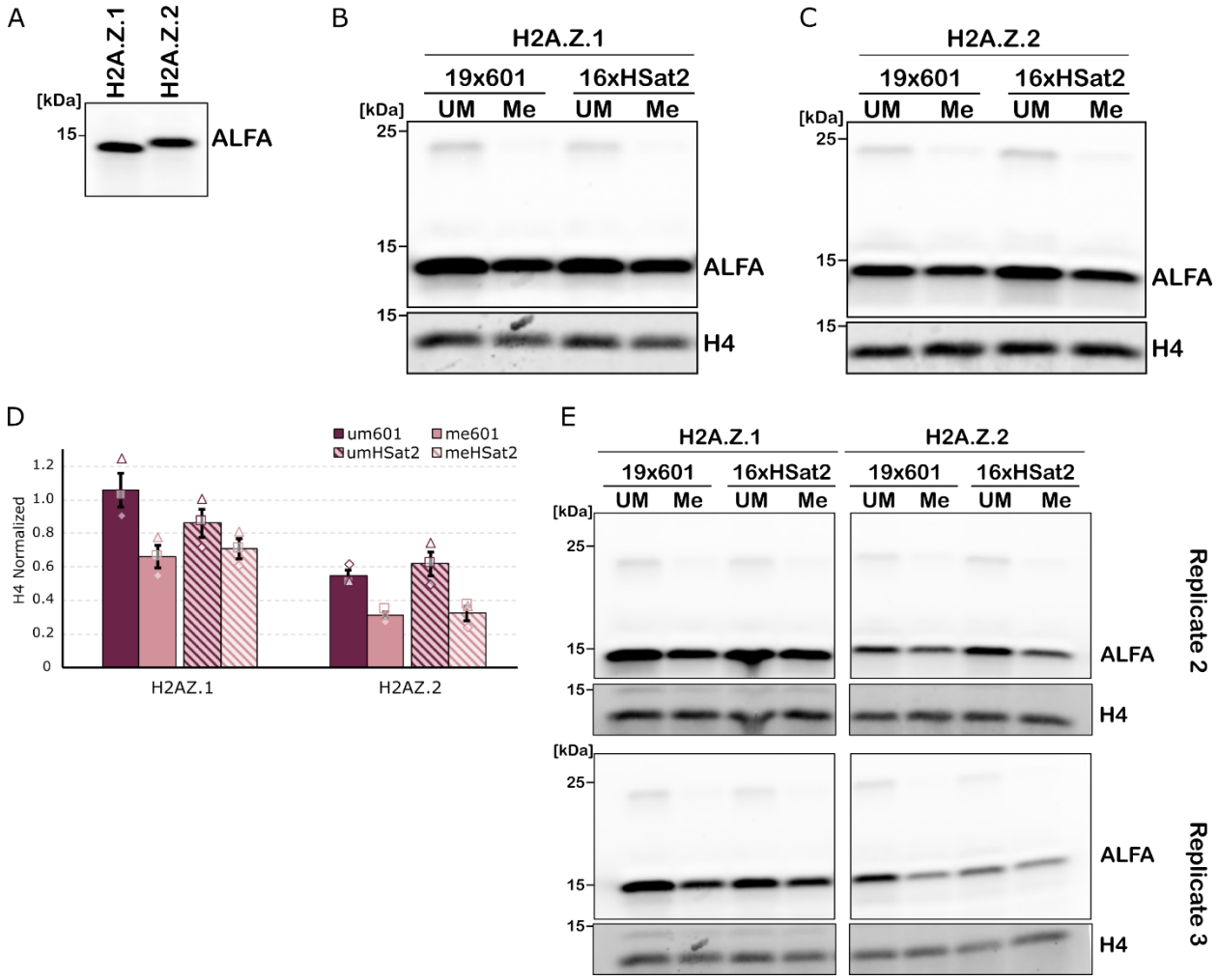

Supplementary Figure 12. Both H2A.Z variants preferentially associate with unmethylated DNA substrates. (A) Expression check of exogenously added mRNA expression for ALFA-tagged versions of both H2A.Z.1 and H2A.Z.2. **(B and C)** Blots of DNA beads incubated with interphase extract expressing either ALFA-tagged H2A.Z.1 **(B)** and H2A.Z.2 **(C).** Presence of the specified H2A.Z variant on DNA beads was determined by blotting against the ALFA-tag with H4 shown as a loading control. **(D)** Quantification of **(B and C)**. ALFA signals were normalized to H4 signals. Unique shapes denote results from three independent experiments (n = 3 biological replicates). Error bars represent SEM. **(E)** Additional replicate blots of data from **(D)**.

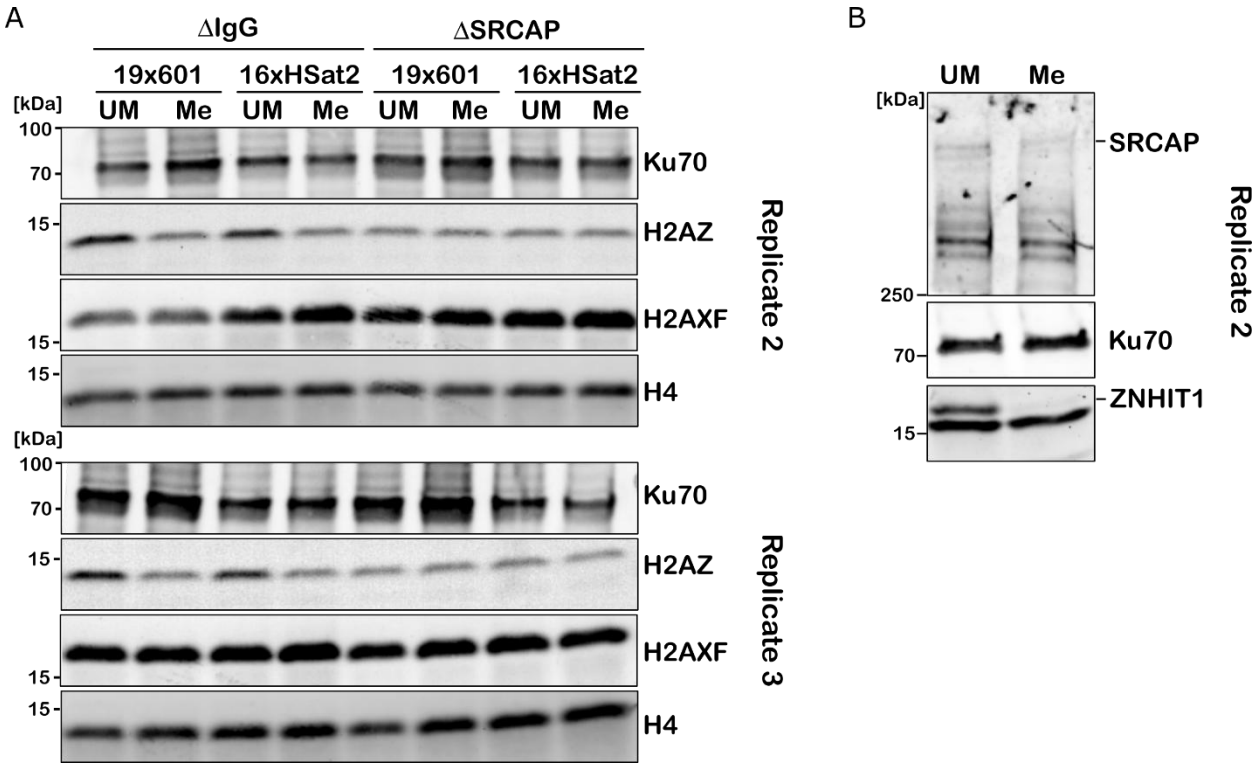

Supplementary Figure 13. Replicates of data from Main Figure 5. (A) Replicate blots of **Main Figure 5B-D**. **(B)** Replicate blots of **Main Figure 5E-F** with Ku70 as a loading control.

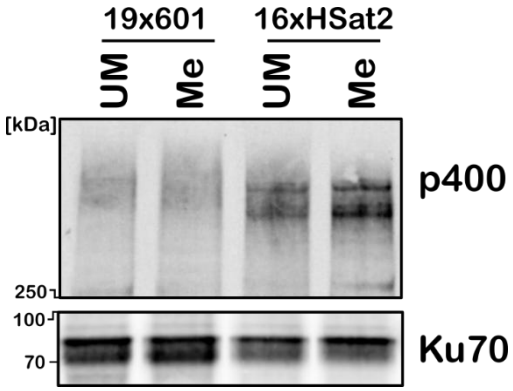

Supplementary Figure 14. Tip60-C does not display DNA methylation sensitivity. Western blots of DNA bead pulldowns from interphase egg extract probing for endogenous p400 (ATPase for Tip60-C) along with respective loading controls.

Supplementary Table 1. Collection and model statistics for the Cryo-EM structures.

Sample	**UM Sat3R-P**	**Me Sat2R-P**	**UM 601L**	**Me 601L**
Data Collection				
Microscope	Titan Krios			
Magnification	81,000			
Voltage (kV)	300			
Camera	Gatan K3			
Electron exposure (e-/Å)	50.703		50	
Defocus range (μm)	-1.5 ~ -3.5			
Pixel size (Å)	0.86			
Micrographs Collected	4544	6891	7020	5427
Data Processing				
Particles (no.)	696,126	566,986	449,178	179,360
Symmetry imposed	C1	C1	C1	C1
Map resolution (Å, FSC = 0.143)	3.05	2.78	3.09	3.25
EMDR ID	***EMD-70474***	***EMD-70473***	***EMD-70480***	***EMD-70481***

	UM Sat2R-P		**Me Sat2R-P**		**601L**	
Atomic Models	**v1**	**v2**	**v1**	**v2**	**UM**	**Me**
Composition						
Chains	10	10	10	10	10	10
Atoms	11117 (Hydrogens: 0)	10905 (Hydrogens: 0)	10585 (Hydrogens: 0)	10558 (Hydrogens: 0)	11101 (Hydrogens: 0)	11477 (Hydrogens: 0)
Residues	Protein: 735 Nucleotide: 259	Protein: 721 Nucleotide: 254	Protein: 701 Nucleotide: 246	Protein: 698 Nucleotide: 246	Protein: 722 Nucleotide: 264	Protein: 738 Nucleotide: 274
Water	0	0	0	0	0	0
Ligands	0	0	0	0	0	0
Bonds (RMSD)						
Length (Å) (# > 4σ)	0.004 (0)	0.003 (0)	0.004 (0)	0.003 (0)	0.003 (0)	0.004 (0)
Angles (°) (# > 4σ)	0.580 (0)	0.525 (3)	0.617 (0)	0.619 (0)	0.578 (1)	0.650 (0)
MolProbity score	1.78	1.47	1.77	1.82	1.6	2.35
Clash score	5.17	4.66	5.86	7.13	8.64	9.79
Ramachandran plot (%)						
Outliers	0	0	0	0	0.14	0
Allowed	2.5	1.56	1.9	2.35	1.56	4.16
Favored	97.5	98.44	98.1	97.65	98.3	95.84
Rama-Z (Ramachandran plot Z-score RMSD)						
whole (N = 719)	1.58 (0.32)	1.80 (0.32)	1.67 (0.32)	1.84 (0.32)	1.99 (0.32)	0.95 (0.30)
helix (N = 518)	2.25 (0.23)	2.33 (0.23)	2.07 (0.23)	2.20 (0.23)	2.25 (0.22)	1.63 (0.22)
sheet (N = 0)	--- (---)	--- (---)	--- (---)	--- (---)	--- (---)	--- (---)
loop (N = 201)	-2.34 (0.36)	-2.21 (0.36)	-2.05 (0.39)	-1.87 (0.38)	-1.43 (0.42)	-2.12 (0.36)
Rotamer outliers (%)	3.44	1.99	3.96	2.94	1.5	5.37
Cβ outliers (%)	NA	NA	NA	NA	NA	NA
Peptide plane (%)						
Cis proline/general	0.0/0.0	0.0/0.0	0.0/0.0	0.0/0.0	0.0/0.0	0.0/0.0
Twisted proline/general	0.0/0.0	0.0/0.0	0.0/0.0	0.0/0.0	0.0/0.0	0.0/0.0
CaBLAM outliers (%)	1.85	1.74	0.9	1.2	1.01	1.42
ADP (B-factors)						
Iso/Aniso (#)	11117/0	10905/0	10585/0	10557/0	11103/0	11477/0
min/max/mean						

Protein	0.00/41.12/5.00	0.28/93.40/15.80	0.23/30.35/4.02	0/89.15/13.38	1.75/82.28/22.40	2.38/89.91/24.49
Nucleotide	0.23/83.07/30.56	3.71/150.32/64.25	-0.00/88.15/40.33	0.06/161.03/73.80	4.85/140.55/59.47	6.08/156.41/67.10
Ligand	---	---	---	---	---	---
Water	---	---	---	---	---	---
Occupancy						
Mean	1	1	1	1	1	1
occ = 1 (%)	100	100	100	100	100	100
0 < occ < 1 (%)	0	0	0	0	0	0
occ > 1 (%)	0	0	0	0	0	0
Box						
Lengths (Å)	79.12, 119.54, 119.54	78.26, 118.68, 118.68	77.4, 116.96, 117.82	77.4, 116.96, 117.82	75.68, 116.1, 122.98	73.96, 116.1, 121.26
Angles (°)	90, 90, 90	90, 90, 90	90, 90, 90	90, 90, 90	90, 90, 90	90, 90, 90
Supplied Resolution (Å)	3.3	3.3	3	3	3.2	3.3
Resolution Estimates (Å)	Masked | Unmasked	Masked | Unmasked	Masked | Unmasked	Masked | Unmasked	Masked | Unmasked	Masked | Unmasked
d FSC (half maps; 0.143)	--- | ---	--- | ---	--- | ---	--- | ---	--- | ---	--- | ---
d 99 (full/half1/half2)	3.5/---/--- | 3.5/---/---	3.5/---/--- | 3.5/---/---	3.2/---/--- | 3.2/---/---	3.2/---/--- | 3.2/---/---	3.3/---/--- | 3.3/---/---	3.4/---/--- | 3.3/---/---
d model	3.4 | 3.4	3.4 | 3.4	3.1 | 3.2	3.1 | 3.2	3.2 | 3.2	3.3 | 3.3
d FSC model (0/0.143/0.5)	2.9/3.1/3.3 | 3.1/3.2/3.3	2.9/3.1/3.3 | 3.0/3.2/3.3	2.6/2.9/3.0 | 2.8/3.0/3.1	2.6/2.9/3.0 | 2.8/3.0/3.1	2.9/3.0/3.2 | 2.9/3.1/3.3	3.1/3.1/3.3 | 3.1/3.2/3.4
Map min/max/mean	-39.16/62.30/0.79	-39.16/62.3/0.82	-41.24/58.89/0.40	-41.24/58.89/0.40	-34.81/61.05/0.68	-31.70/51.07/0.56
Model vs Data						
CC (mask)	0.86	0.88	0.83	0.83	0.82	0.8
CC (box)	0.78	0.78	0.7	0.68	0.74	0.7
CC (peaks)	0.75	0.75	0.68	0.66	0.7	0.65
CC (volume)	0.8	0.82	0.75	0.76	0.78	0.76
Mean CC for ligands	---	---	---	---	---	---
PDB ID	***9OGS***	***9OGZ***	***9OGR***	***9OH0***	***9OH1***	***9OH2***

Supplementary Table 2. Alignment statistics of CnT-BS sequencing libraries. XTC reads were downsampled to 30 million reads to match sperm samples, then all raw reads were trimmed and deduplicated using fastp v0.24.0 and aligned to the *Xenopus* laevis genome (Xenla 10.1) or lambda genome (to assess for bisulfite conversion efficiency) using Bismark v0.24.2. Methylated CpG percentages for H2A.Z samples were determined for the top 2.5 % of H2A.Z peaks by AUC (obtained using SEACR v1.3) while methylated percentages for H3 associated CpGs was conducted on regions outside of determined H2A.Z peaks. All CpGs met a cutoff of at least 5 reads to be counted. Methylated lambda CpG statistics were calculated from all mapped CpGs with no filtering.

		Alignment to Xenopus laevis			*Alignment to lambda*	
		Aligned %	**Total Aligned Reads (No.)**	**Methylated CpG %**	**Aligned %**	**Methylated CpG %**
Sperm Pronuclei						
H3	*Rep 1*	71.7	24141516	**85.6**	0.8	**0.6**
	Rep 2	71.0	24185147	**85**	1.0	**0.6**
H2AZ	*Rep 1*	64.7	25362485	**42.5**	4.0	**0.6**
	Rep 2	69.0	21963635	**43.5**	2.5	**0.6**
XTC-2						
H3	*Rep 1*	68.2	19539297	**53.2**	7.2	**0.4**
	Rep 2	62.4	17758471	**53.8**	15.9	**0.3**
H2AZ	*Rep 1*	69.1	19409396	**3.2**	12.4	**0.3**
	Rep 2	70.9	20109208	**2.8**	9.8	**0.3**

Supplementary Table 3. Fragment statistics of filtered genomic bins used for sequencing analysis. A count matrix was generated from processed bam files over 1,000 bp bins of the *Xenopus laevis* genome. Mitochondrial reads and bins containing fewer than 17 reads across less than 2 samples were removed to filter out low signal areas. Replicates for each sample were averaged and resulting count matrix used for genomic annotation analysis.

		Fragments in Bins (No.)	Fragments in Bins (%)
Sperm Pronuclei			
H3	*Rep 1*	9062125	34.04
	Rep 2	9265292	34.68
H2AZ	*Rep 1*	11482371	43.04
	Rep 2	9213698	39.58
XTC-2			
H3	*Rep 1*	7789646	36.43
	Rep 2	8145900	41.79
H2AZ	*Rep 1*	14276029	66.62
	Rep 2	15187573	69.13
Total Bins (No.)		506009	